THESIS

EXTREME POST-WILDFIRE FLOODING IN THE COLORADO FRONT RANGE

Submitted by

Daniel Joseph Brogan

Department of Civil and Environmental Engineering

In partial fulfillment of the requirements

For the Degree of Master of Science

Colorado State University

Fort Collins, Colorado

Fall 2014

Master's Committee:

Advisor: Peter A. Nelson

Brian P. Bledsoe
Lee H. MacDonald
Ellen E. Wohl

ABSTRACT

EXTREME POST-WILDFIRE FLOODING IN THE COLORADO FRONT RANGE

In 2012, the High Park Fire near Fort Collins, Colorado burned ~353 km^2 and destroyed 259 structures. After the fire, the ungaged 15.5 km^2 Skin Gulch watershed experienced two geomorphically effective floods. Here, we investigate connections among storm characteristics, flood response, and geomorphic change by characterizing the hydrometeorology, peak flood discharge, and channel changes for these two extreme events. Our specific objectives were to: 1) to quantify spatial patterns of total rainfall and maximum 15-minute intensity for each storm by using local rain gages and Doppler radar; 2) to estimate the peak discharge and the corresponding uncertainty for each event using several modeling techniques; and 3) to interpret the rainfall-runoff response for these storms in the context of spatial interaction of precipitation, burn severity, runoff, and geomorphic change. Precipitation was estimated with bias-corrected radar observations, and at-a-station, 1D, and 2D hydraulic modeling calculations were used to characterize the peak discharge for each flood, calibrated to surveyed high water marks. The first storm occurred on 6-7 July 2012, just days after the fire was extinguished, when a convective thunderstorm produced total rainfall of ~50 mm with a maximum 15-minute intensity of ~60 mm/h over a portion of Skin Gulch that was burned at high severity. The resulting flood caused considerable deposition in the channel and 2D hydraulic calculations suggest the peak discharge was 70-120 m^3/s. The following summer, from 9-15 September 2013, a very unusual multi-day storm produced 279 mm, which represents a recurrence interval greater than 1000 years. The peak 15-minute rainfall intensity for this storm estimated by the radar was about 100 mm/h,

although the highest 15-minute intensity recorded by a rain gage was 38 mm/h. Based on 2D flow analysis, the peak discharge for this flood was <50 m^3/s. Although the peak discharge was lower than that of the 2012 flood, this flood produced comparable channel change due to its extended duration. Both events rank among the largest rainfall-runoff floods per unit area ever recorded in the continental United States, and point to the dramatic effects wildfire can have on storm hydrology and channel morphology.

ACKNOWLEDGEMENTS

I would personally like to thank my academic adviser, Dr. Peter Nelson for all the guidance and support through the entire process of my thesis work. Additionally, many thanks go to Dr. Lee MacDonald for his wisdom in the field and constantly asking logical questions that get at the root of processes. In addition to Peter and Lee, I would like to thank Dr. Brian Bledsoe and Dr. Ellen Wohl for their feedback on my research and their comments on this thesis. Much appreciation is due to Dr. James A. Smith and Mary Lynn Baeck from Princeton University for providing us with the 15 min HydroNEXRAD data product for the July 2012 storm event. I also would like to acknowledge all the people that helped me in the field, the countless hours of assistance they provided was invaluable. Field assistants listed alphabetically by last name include: Doug Bailey, Justin Blumenthal, Andy Brew, Amy Brogan, Esker Brogan, Jeff Cadry, Steven Filippelli, Blaine Hastings, Aaron Havel, David Kamin, Luke McNally, Sam Michels-Boyce, Jacob Morgan, Tyler Rosburg, Cassidi Rosenkrance, Jason Roudebush, and Joel Sholtes.

Most of the funding for this project came from a National Science Foundation grant and I am very grateful for this. Much appreciation goes to the Arapaho-Roosevelt National Forest for permitting us to work within the National Forest.

Lastly, the most important person I want to acknowledge is my lovely wife, Amy. She was incredibly supportive through everything and remained calm even when times were extremely stressful. Amy spent many hours helping me in the field, providing suggestions, and reviewing this and many other documents. You are the best and I love you dearly!

TABLE OF CONTENTS

ABSTRACT ii
ACKNOWLEDGEMENTS iv
TABLE OF CONTENTS v
LIST OF TABLES vi
LIST OF FIGURES vii
1. INTRODUCTION 1
2. SITE DESCRIPTION AND BACKGROUND 4
3. METHODS 7
3.1. FIELD OBSERVATIONS 7
3.2. PRECIPITATION 9
3.3. PEAK FLOW MODELING 12
3.3.1. LIDAR DATA AND MODEL DOMAINS 12
3.3.2. SLOPE-AREA METHOD 14
3.3.3. CRITICAL FLOW METHOD 15
3.3.4. HEC-RAS MODELING 15
3.3.5. TWO-DIMENSIONAL MODELING 19
4. RESULTS 21
4.1. PRECIPITATION 21
4.2. PEAK FLOWS 24
4.2.1. SLOPE-AREA METHOD 24
4.2.2. CRITICAL FLOW METHOD 31
4.2.3. HEC-RAS MODELING 31
4.2.4. NAYS2D MODELING 34
4.3. SUMMARY OF PEAK FLOW CALCULATIONS 37
5. DISCUSSION 39
5.1. RECREATING EXTREME FLOODS 39
5.2. COMPARISON OF THE 2012 AND 2013 EVENTS 42
6. CONCLUSIONS 46
7. REFERENCES 47
8. APPENDIX 54

LIST OF TABLES

Table 1. Percentages of burn severity level for Skin Gulch computed from the vegetation burn severity map shown in Figure 1. 6
Table 2. Mean field bias (MFB) for the radar data during the 2012 and 2013 floods. 21
Table 3. Critical flow results presented in m^3/s for the 2012 survey data, and the 2013 before and after September flood survey data 31
Table 4. Summary table of peak discharge values 38

LIST OF FIGURES

Figure 1. Top: Elevation map of the Cache la Poudre watershed in the Colorado Front Range. Lower left: Vegetation burn severity map of the High Park Fire. Lower right: The Skin Gulch watershed, with vegetation burn severity overlain on a shaded relief map. Black dots show locations of rain gages used for radar bias correction. 4
Figure 2. Map of individual cross-sections (XS), high water marks, and hydraulic model boundaries. 8
Figure 3. High water marks as seen on (a) 22 July 2012 and (b) 24 September 2013. 9
Figure 4. LiDAR comparison for XS9 illustrating (a) pre- and post-2013 NEON LiDAR correction, and (b) corrected LiDAR elevations for XS9 compared to the RTK-GPS elevations. 13
Figure 5. Cross-sections used in HEC-RAS modeling of the 2012 event. 18
Figure 6: (a) Total precipitation in mm, and (b) maximum 15-min rainfall intensity estimates in mm/h for 6-7 July 2012 17:30 UTC to 7 July 2012 13:00 UTC using Hydro-NEXRAD. (c) Total precipitation in mm, and (d) maximum 15-min rainfall intensity estimates in mm/h for 9-15 September 2013 using DAA data. Crosses indicate locations of precipitation gages. . 22
Figure 7. Bias-corrected 15-minute rainfall intensity for each radar pixel within SG for the (a) 2012 storm; and (b) the 2013 storm. 23
Figure 8. Decrease in predicted discharge with an increase in Manning's roughness coefficient for the slope-area method for: a) 2012 post-flood, b) 2013 pre-flood, and c) 2013 post-flood 25
Figure 9. (a) LWD pushed against standing tree near XS6, and (b) imbricated boulders above channel bed between XS8 and XS9. 27
Figure 10. Photos looking downstream at XS4, with (a) being prior to the September 2013 flood, and (b) the same location after the flood. Note the same tree in the upper left of both pictures and the slope failure along the hillslope to the right. 29
Figure 11. Pre- and post-2013 flood cross-section elevation comparisons and photos looking downstream for (a) XS8, and (b) XS4. Note the general trend of incision, and incision plus widening in the downstream direction. Photos taken on 24 September 2013. 30
Figure 12. Graphs illustrating the RMSE from HEC-RAS for combinations of *Q* and *n* for: a) 2012 NEON, b) 2013 NEON, and 3) 2013 FEMA. The best discharge estimate for a given roughness value is that which minimizes the RMSE. 33
Figure 13. Graphs illustrating the RMSE from Nays2D for combinations of *Q* and *n* for: a) 2012 NEON, b) 2013 NEON, and 3) 2013 FEMA. 35
Figure 14. Example superelevation water surface profile for the 2012 flood. Note the vertical exaggeration of the y-axis. 36
Figure 15. Patterns of shear stress (in Pa) for the 2012 flood Nays2D model using a combination of n=0.10 and Q=70 m^3/s. 37
Figure 16. Location of Froude numbers below 0.8, from 0.8 to 1.2, and greater than 1.2 for the 2013 post-flood topography analysis for the Nays2D combination of n=0.06 and Q=30 m^3/s. 40
Figure 17. Range of peak discharges with the lowest RMSE values from Nays2D for the 2012 and 2013 flood events in SG plotted with the largest rainfall-runoff floods experienced in

the United States and Puerto Rico [modified from *O'Connor & Costa*, 2004]. The blue and red lines correspond to the ~90th and ~99th percentiles. Inset map [from O'Connor and Costa, 2004] shows the locations of watersheds contributing to the plot, and the red X indicates the location of SG..... 43

1. INTRODUCTION

After a wildfire, watersheds are extremely vulnerable to geomorphic change and flooding due to the altered physiographic properties of the landscape [e.g. *Roering & Gerber*, 2005; *Shakesby & Doerr*, 2006; *Bowman et al*., 2009]. Wildfires are occurring more frequently in the Western United States and at higher intensities as a result of earlier onset of snowmelt [*Westerling et al.*, 2006] and historic wildfire suppression [*Keane et al.*, 2002]. Larger post-fire flood peaks [*Moody & Martin*, 2001b] and increased sediment production [*Morris & Moses*, 1987; *Meyer et al.*, 1995; *DeBano et al.*, 1996; *DeBano*, 2000; *Robichaud et al*., 2000; *Benavides-Solorio & MacDonald*, 2001; *Meyer et al.*, 2001; *Moody & Martin*, 2001a; *Benda et al*., 2003] lead to potentially adverse effects to water quantity, water quality, aquatic habitat suitability, and reservoir sedimentation [*Rinne*, 1996; *Dunham et al.*, 2003; *Rhoades et al.*, 2011]. This in turn impacts the water quantity and the quality of water supplied to municipalities, agriculture, and the ecosystem [*Moody & Martin*, 2001a; *Robichaud et al.*, 2000; *Burton*, 2005].

Post-wildfire increases in runoff and soil erosion are controlled by burn severity, soil water repellency, a reduction in surface cover [*Neary et al.*, 1999; *DeBano*, 2000; *Huffman et al.*, 2001; *Moody et al.*, 2008; *Larsen et al.*, 2009], and changes in soil properties due to the reduction in soil organic matter [*Shakesby and Doerr*, 2006]. These changes combine to cause a large reduction in the intensity threshold at which precipitation initiates Horton overland and hillslope-scale surface erosion [*Morris & Moses*, 1987; *Moody & Martin*, 2001a, 2001b; *Wondzell & King*, 2003; *Benavides-Solorio & MacDonald*, 2005; *Larsen & MacDonald*, 2007] . Within the riparian corridor, the burning of vegetation can lead to reduced floodplain roughness and bank stability, leading to a reduction in the threshold for channel change [e.g., *Church*,

2002]. Geomorphic changes due to wildfires have legacy effects that last from tens to thousands of years [*Meyer et al.*, 1992; *Meyer et al.*, 1995; Elliott and Parker, 2001; *Moody & Martin*, 2001a; *Legleiter et al.*, 2003].

In the western United States, flooding that occurs after wildfire is often caused by localized, short-duration convective thunderstorms, which can display strong spatial gradients in the maximum 30-minute rainfall intensity [e.g., *Moody and Martin*, 2001a, 2001b]. The spatial variability in precipitation interacts with the channel network and spatial pattern of burn severity to produce nonlinear geomorphic responses [*Moody and Martin*, 2009]. Indirect estimates of peak discharge require highly detailed and well planned post-flood surveys of channel topography and high water marks [*Borga et al.*, 2008], which can then be used in calculations and hydraulic models. Model-predicted peak flows are subject to uncertainty associated with estimates of the hydraulic roughness parameter [e.g., *Miller and Cluer*, 1998; *Wohl*, 1998], as well as uncertainty in the topographic input data [e.g., *Marks & Bates*, 2000; *Cook & Merwade*, 2009]. Intra-event channel change aggradation or erosion can greatly increase the uncertainty of peak flow calculations; however, these uncertainties in indirect discharge estimates are frequently overlooked.

Two recent extreme post-wildfire floods in the Colorado Front Range provide an opportunity to investigate connections between wildfire burn severity, storm characteristics, flood response, and geomorphic change for two different types of precipitation events. In June 2012 the High Park Fire (HPF) burned 353 km^2 near Fort Collins, Colorado, making it the third largest fire in Colorado's recorded history. On 6-7 July 2012, just a few days after the fire was contained, a localized convective thunderstorm over a region of high burn severity in the ungaged Skin Gulch (SG) watershed caused considerable in-channel deposition and transport of

cobble- to boulder-sized material. The following summer the central and northern Colorado Front Range experienced an unusually large and long-duration storm from 9-15 September 2013 that caused incision, channel widening, and a general reworking of sediment in SG. Our field observations following these events suggested that: 1) the storms differed drastically in total precipitation and spatial patterns of maximum intensity, 2) the July 2012 flood was primarily depositional while the September 2013 event was primarily erosional, and 3) both precipitation events had a geomorphically effective impact on the SG watershed [sensu *Baker & Costa*, 1987; *Costa & O'Connor*, 1995; *Miller*, 1995].

The goal of this work is to evaluate post-fire runoff response and peak discharge for these two very different precipitation events, and to address the uncertainties associated with roughness and topographic changes during the flood on indirect discharge calculations. Our specific objectives were to: 1) to quantify spatial patterns of total rainfall and maximum 15-minute intensity for each storm by using local rain gages and Doppler radar; 2) to estimate the peak discharge and the corresponding uncertainty for each event using several modeling techniques; and 3) to interpret the rainfall-runoff response for these storms in the context of spatial interaction of precipitation, burn severity, runoff, and geomorphic change.

2. SITE DESCRIPTION AND BACKGROUND

On 9 June 2012, a lightning strike ignited the HPF, which ultimately burned 353 km^2 and destroyed more than 259 homes [*HPF BAER Report*, 2012]. At the time, the HPF was the second largest wildfire in Colorado's history. The HPF burn area is located roughly 25 km west of Fort Collins, Colorado in the middle elevation range (1,586 m to 3,142 m above sea level) of the Cache la Poudre River (CLP) watershed (Figure 1).

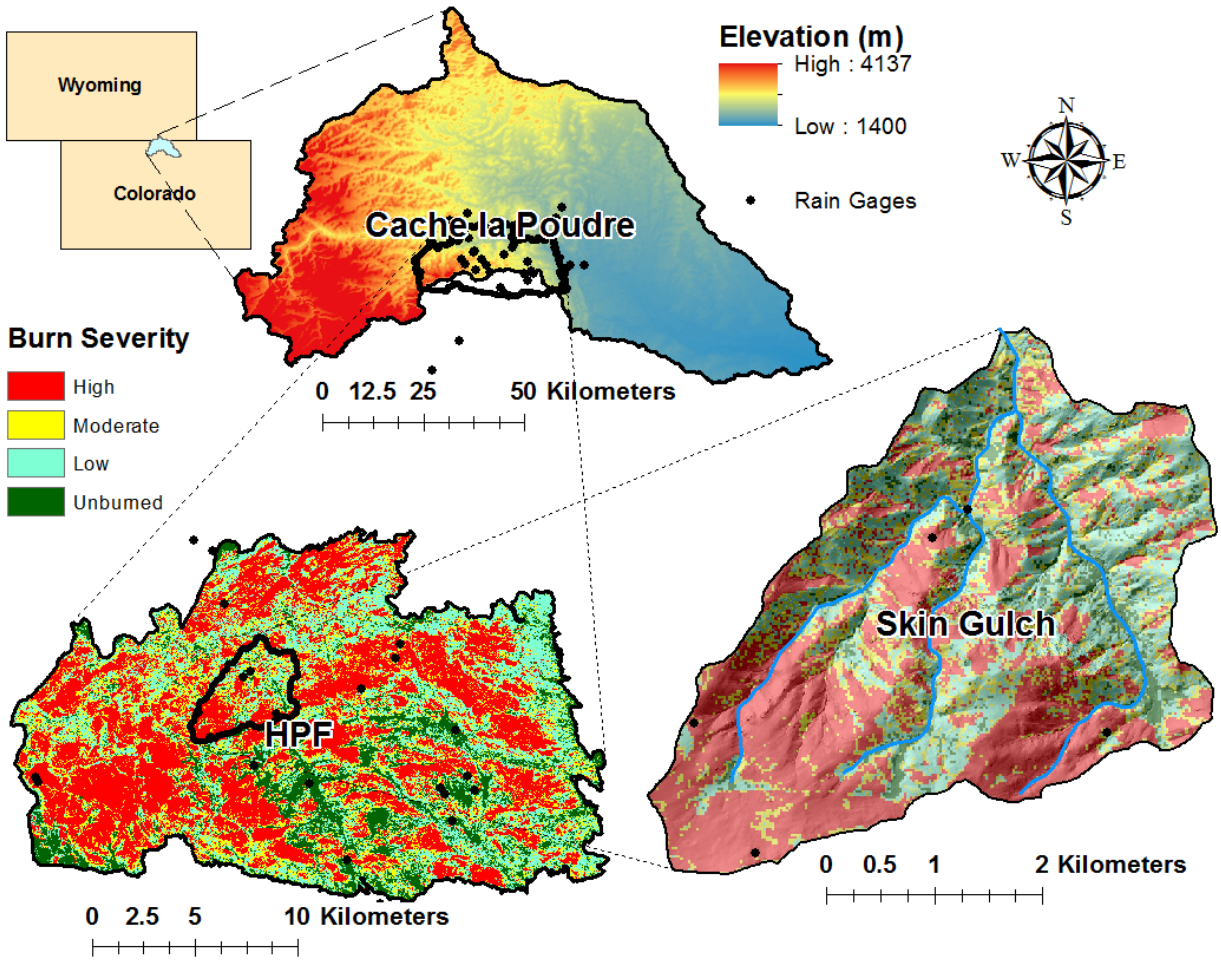

Figure 1. Top: Elevation map of the Cache la Poudre watershed in the Colorado Front Range. Lower left: Vegetation burn severity map of the High Park Fire. Lower right: The Skin Gulch watershed, with vegetation burn severity overlain on a shaded relief map. Black dots show locations of rain gages used for radar bias correction.

The SG watershed was the primary study site for this research and is 15.5 km^2 in size, ranges in elevation from 1890 m to 2580 m, and drains northwards into the Cache la Poudre River near the intersection of Colorado Highway 14 and Stove Prairie Road. Pre-wildfire the vegetation in SG was 81% evergreen forest (ponderosa pine) 15% shrub/scrub (lower montane-foothill shrubland), and ~4% deciduous forest, grassland/herbaceous and woody wetland (data derived from the 2011 National Land Cover Database [Jin et al., 2013]). The geology of Skin Gulch is primarily Precambrian metasedimentary and metaigneous schists, gneisses, and plutonic igneous rocks [*Abbott*, 1970]. SG was a narrow ~1 m wide channel and flow was ephemeral prior to burning (P. Cole, pers. comm., 2014). Peak flows in the region are predominantly snowmelt driven above ~2,300 m elevation and rain generated below ~2,300 m [*Jarrett & Costa*, 1988].

SG burned primarily at high severity (Figure 1; Table 1). Vegetation burn severity was classified by a multistage decision tree, and was trained using photo interpreted classes from the 20 July 2012 ~5 m RapidEye imagery dataset (B. Stone, Colorado State University, pers. comm., 2014). The four vegetation burn severity classes are: unburned; low severity, where the understory vegetation was consumed by the fire but the majority of the upper canopy was unscorched; moderate severity, where the needles were killed but not fully consumed; and high severity, where the understory and canopy were completely consumed [*Ryan and Noste*, 1985; *Keeley*, 2009]. The final 25 m data product was validated using independent field data and compared against similar severity maps, such as the Burned Area Reflectance Classification (BARC) and Rapid Assessment of Vegetation Condition after Wildfire (RAVG) (B. Stone, Colorado State University, pers. comm., 2014).

Table 1. Percentages of burn severity level for Skin Gulch computed from the vegetation burn severity map shown in Figure 1.

Burn severity	Skin Gulch
Unburned/very low	6.4%
Low	29.0%
Moderate	20.9%
High	43.6%

3. METHODS

3.1. FIELD OBSERVATIONS

Field surveys post-wildfire in 2012 and 2013 characterized channel geomorphic changes and recorded high water marks from floods in the lower portion of the main channel and its largest tributary (Figure 2). The only channel morphologic data collected prior to any post-fire storms was a cross-section near the outlet of SG established on 4 July 2012 (XS1 in Figure 2). This cross-section was resurveyed on 22 July 2012. During the latter part of the summer nine additional cross-sections were established to monitor post-wildfire geomorphic changes (XS2 – XS10 in Figure 2). Cross-section endpoints were permanently monumented by metal rebar. At each cross-section a longitudinal profile was surveyed that was centered at the cross-section and extended about 7-8 times the channel width at base flow. The initial surveys in 2012 were completed using an autolevel and stadia rod or a Leica TCR407 total station, while the surveys in 2013 were completed with a Topcon GR-5 Real-Time Kinematic Global Positioning System (RTK-GPS). The estimated the accuracy of the autolevel surveys is less than 1 cm vertically and 2 cm horizontally, while the lateral and vertical accuracy of the total station is estimated to be <3 cm. The RTK-GPS resulted in a maximum horizontal root mean square (RMS) of 0.05 m and a maximum vertical RMS of 0.08 m between the static data collected by the base station and the survey points taken with the RTK-GPS.

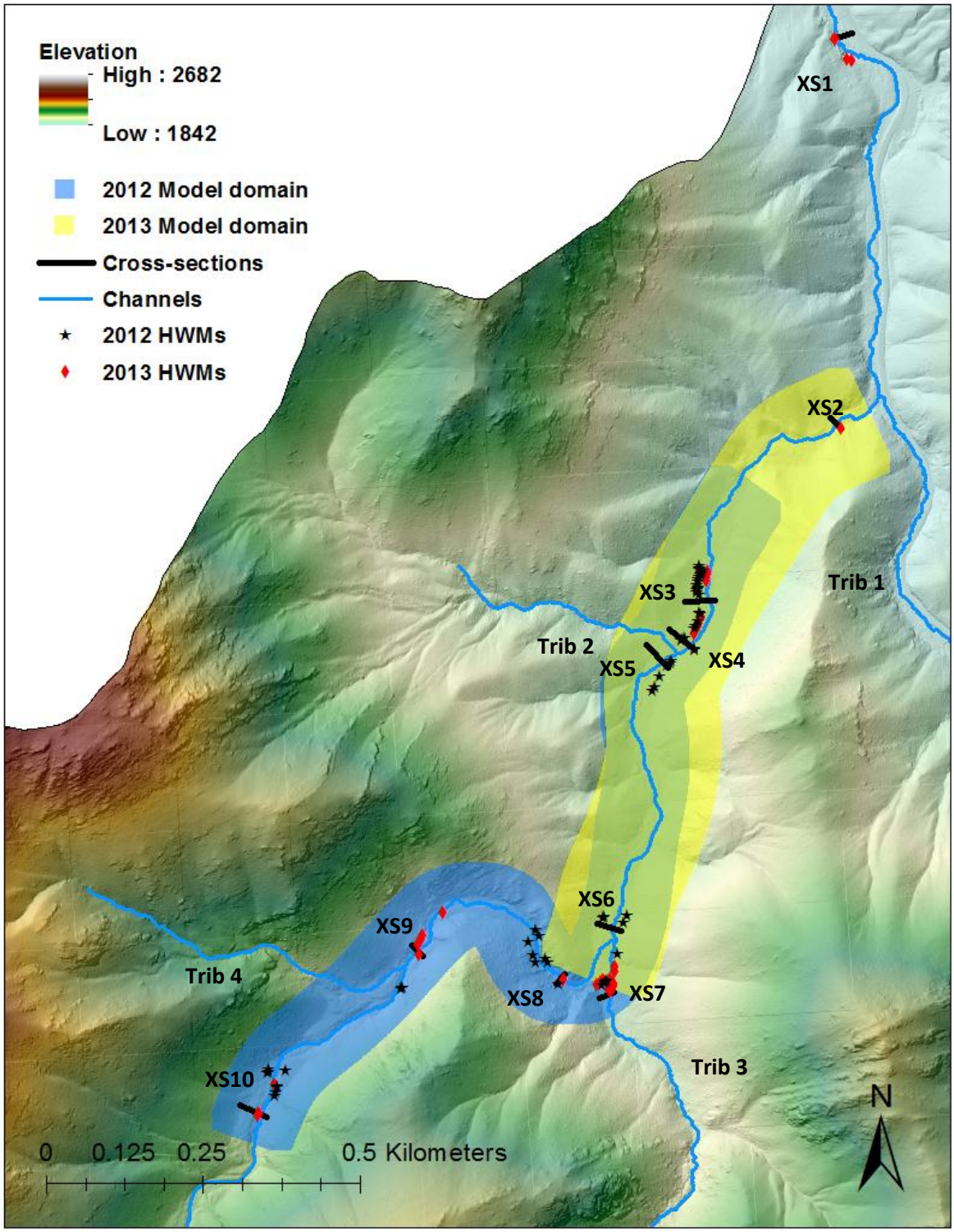

Figure 2. Map of individual cross-sections (XS), high water marks, and hydraulic model boundaries.

Fifty-three high water marks (HWMs) were surveyed in September 2012 and used to model the July 2012 flood. Forty-two HWMs were surveyed after the September 2013 flood. HWMs for the 2012 flood primarily consisted of deposited ash and fine debris along the channel margins, while the primary HWM indicator following the 2013 flood was matted down vegetation (Figure 3). Several of the 2012 HWMs remained after the 2013 flood, and these indicated that the 2012 HWMs were at a higher elevation than the 2013 HWMs. Large imbricated cobbles and boulders were observed in portions of the SG channel following the 2012 flood, indicating that these grains had been mobilized during the flood. The intermediate axes of 60 of these particles were measured with a tape measure. An ultrasonic depth sensor was installed during the spring of 2013 and collected data during the 2013 flood. These data were used to estimate the duration of the flood.

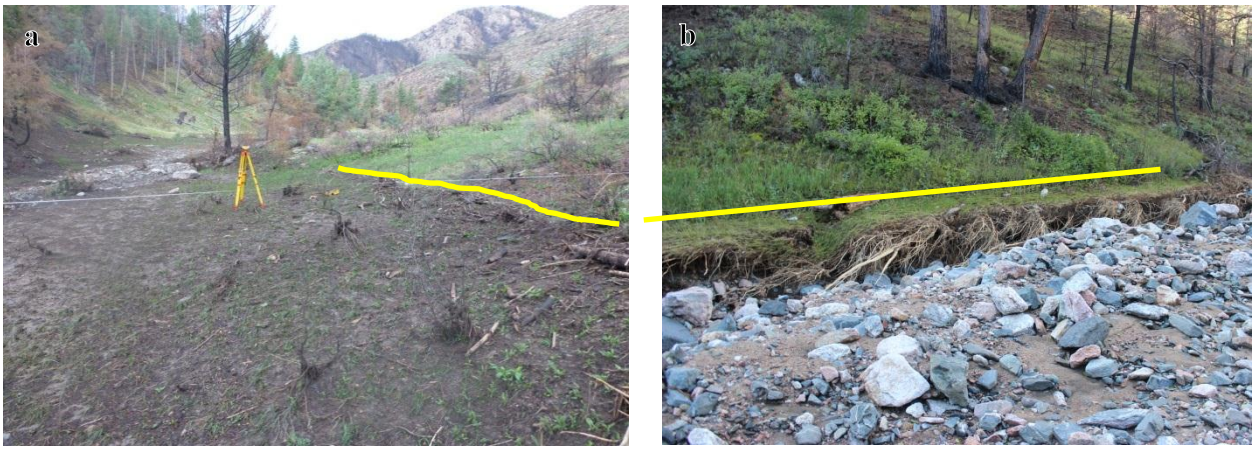

Figure 3. High water marks as seen on (a) 22 July 2012 and (b) 24 September 2013.

3.2. PRECIPITATION

Precipitation is one of the most difficult physical parameters to characterize for large runoff events due to the potentially high spatial variability and limited number of rain gages [*Gerbremichael & Krajewski*, 2004]. The rainfall from the 6-7 July 2012 and 9-15 September 2013 storms were characterized by combining radar data with rain gage measurements to

produce a bias-corrected precipitation product with greater spatial and temporal resolution than could be achieved with just the rain gage data. Sixteen rain gages were used to correct the radar data for the 2012 storm and 43 rain gages were used for the 2013 storm. The 2012 rain gages include only daily rainfall totals from the Community Collaborative Rain, Hail and Snow Network (CoCoRaHS) [*Cifelli et al.*, 2005]. For the 2013 storm there were seven more CoCoRaHS gages, 14 tipping bucket rain gages with a resolution of 0.01 inch (0.254 mm), one of NOAA's Global Historical Climatology Network weather stations, and five United States Geological Society (USGS) telemetered gages.

Radar data used in the analysis were collected by the National Weather Service WSR-88D NEXRAD Doppler radar in Cheyenne, Wyoming (KCYS). In October 2012, the KCYS radar was upgraded from single to dual polarization [*Martin*, 2013], which allows for more complex algorithms and improved precipitation estimates [*Seliga & Bringi*, 1976; *Ryzhkov & Zrnic*, 1996a, 1996b; *Fulton et al.*, 1998]. Due to this change in radar technology between the 2012 and 2013 storms, two approaches were used to determine the hydrometeorologic conditions for each storm.

We used the 15-minute Hydro-NEXRAD products for the 2012 storm [*Krajewski et al.*, 2011] generated from the KCYS radar and gridded in ~1 km^2 bins. The 2013 storm was characterized using the KCYS dual-polarization one-hour digital accumulation array (DAA) from the NOAA National Climatic Data Center's Hierarchical Data Storage System. This had a radial grid of 0.13 nautical mile x 1 degree resulting in a spatial resolution of ~0.5 km^2 bins over the SG watershed and an average temporal resolution of 5 min 43 sec.

Both radar datasets were corrected using a daily mean field bias (MFB) based on local precipitation gages to better capture the spatial and temporal structure of extreme rainfall [*Smith*

et al. 2005; *Wright et al.* 2013]. The bias correction was computed from the daily precipitation values for each precipitation gage and the corresponding pixel of the radar. The daily MFB correction was calculated as:

$$B_i = \frac{\sum G_{ij}}{\sum R_{ij}} \quad \text{(Eq. 1)}$$

where B_i is the bias for a particular day *i*, G_{ij} is the daily rainfall for day *i* and gage *j*, and R_{ij} is the 24 hour rainfall for day *i* and the radar pixel containing gage *j* [*Wright et al.*, 2013]. Because the CoCoRaHS gages are collected at 0700 local time, all daily totals and MFB calculations represent the 24-hour period ending at 0700. The MFB was then applied to each radar scan collected that day; the daily total precipitation was recomputed and the 15-minute rainfall intensities were determined for 2012 and interpolated from the inter-daily time steps for 2013. A bias was applied only if 5 or more radar-rain gage pairs registered nonzero precipitation for a given day, and the maximum bias was set to six [*Wright et al.*, 2013].

The duration of the July 2012 storm was determined according to the National Weather Service's definition of "Storm Total Precipitation," which defines a storm by at least a one-hour break in precipitation. The precipitation window for the HydroNEXRAD data was 6 July 2012 1730 UTC to 7 July 2012 1300 UTC. The precipitation window for the second storm was set to 0700 MDT 9 September 2013 to 0700 MDT 15 September 2013 in order to be consistent with preliminary assessments of the storm [*Lukas et al.*, 2013]. Using the processed radar data, maps of the maximum 15-minute intensities measured at each radar pixel over the duration of the storm were created to show the spatial variability in precipitation over SG.

3.3. PEAK FLOW MODELING

The peak discharges for the two floods were calculated using four methods, and in order of increasing complexity these were: 1) slope-area, 2) critical flow, 3) one-dimensional hydraulic modeling, and 4) two-dimensional hydraulic modeling. These methods and the topographic input data they required are described below.

3.3.1. LIDAR DATA AND MODEL DOMAINS

Three airborne LiDAR topographic datasets covering the SG watershed have been collected since the HPF. The National Ecological Observatory Network (NEON) Airborne Observation Platform collected LiDAR data in October 2012 and July 2013, and the USGS and FEMA obtained LiDAR one month after the September 2013 flood. The primary product from each flight was a 1-m bare-earth digital elevation model (DEM).

Data from the NEON flights was projected in UTM Zone 13 North, WGS84 (ITRF2000 reference frame), with orthometric heights in NAVD88 based on GEOID12A. The FEMA/USGS data used UTM Zone 13 North, NAD83 (2011) and orthometric heights in NAVD88 based on GEOID12A. Due to possible errors transforming between the NAD83 and WGS84 ellipsoids within NEON's LiDAR processing software, Optech LiDAR Mapping Suite, and a lack of vertical ground control, the DEMs required a mean bias correction (i.e., elevation adjustment) to fit our surveyed cross-sections. After this correction, the root-mean-square error (RMSE) between surveyed GPS points and the LiDAR surfaces averaged 0.126 m (n=2575) for the 2012 NEON DEM and 0.187 m (n=2437) for the 2013 NEON DEM. The 2013 USGS LiDAR had an average RMSE of 0.239 m (n=3060). After adjustment, the DEMs and the survey data showed satisfactory agreement (e.g., Figure 4).

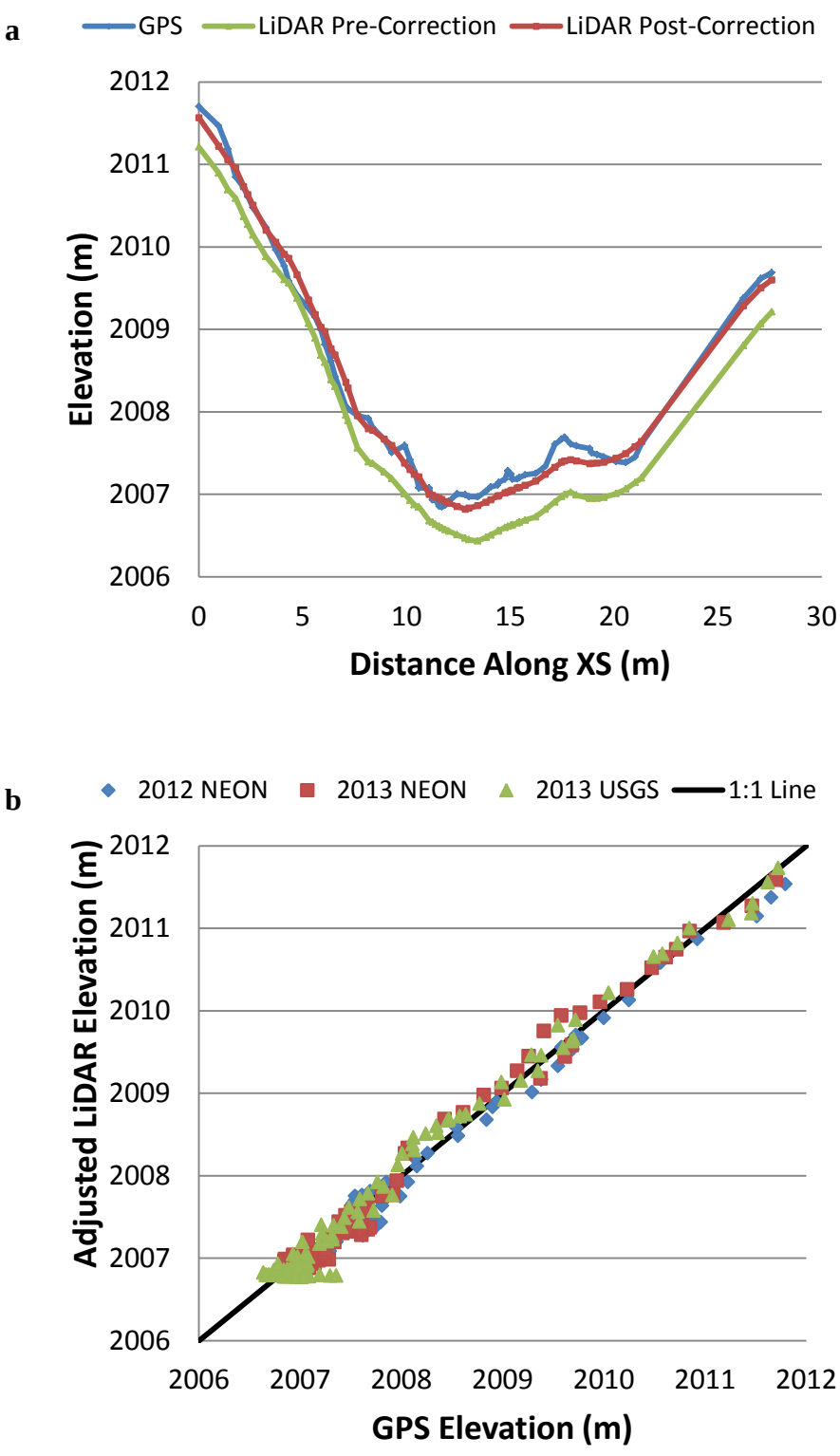

Figure 4. LiDAR comparison for XS9 illustrating (a) pre- and post-2013 NEON LiDAR correction, and (b) corrected LiDAR elevations for XS9 compared to the RTK-GPS elevations.

A field visit after the 2012 storm suggested that only the western tributary and main stem of Skin Gulch experienced flood flows, and that contributing flows from tributaries were negligible as indicated by the lack of HWMs. Thus the domain for modeling this flood extended upstream to incorporate the HWMs around XS10, where the drainage area is ~4.7 km^2 (Figure 2). In contrast, the 2013 flood had considerable flow contributions and geomorphic change within tributaries 1 and 3. Thus, the domain for modeling this flood was restricted to the channel between the confluences of tributary 1 and tributary 4 (Figure 2). The upstream drainage area at the confluence just upstream of XS6 is ~8.17 km^2.

3.3.2. SLOPE-AREA METHOD

The slope-area method uses Manning's equation to estimate the flood discharge as defined by the high water marks. Manning's equation in metric units is:

$$Q = VA = \frac{AR^{2/3}\sqrt{S}}{n} \qquad \text{(Eq. 2)}$$

where Q is the discharge (m^3/s), *V* is the mean cross-sectional averaged velocity (m/s), *A* is the cross-sectional area of the flow (m^2), *R* is the hydraulic radius (m), *S* is the mean water surface slope (m/m), and *n* is Manning's roughness coefficient ($s/m^{1/3}$).

(Eq. 2 was only applied to surveyed cross-sections with nearby measured HWMs. For the July 2012 flood this included cross-sections 3, 4, 5, and 8. For the pre-2013 flood and post-2013 flood Manning's equation was used at cross-sections 2, 7, 9, and 10. For each calculation *S* was estimated from the surveyed longitudinal profile of the bed slope, and both *R* and *A* were computed from the surveyed cross-section and HWM. Since *n* is an unknown parameter, a range

of peak discharges was calculated for each flood by varying *n* from 0.03 to 0.10 in increments of 0.01 [*Barnes*, 1967; *Limerinos*, 1970; *Dingman & Sharma*, 1997],

3.3.3. CRITICAL FLOW METHOD

In steep channels and paleohydrologic studies [e.g. *Grant*, 1997; *Webb and Jarrett*, 2002] peak discharge is sometimes estimated by assuming critical flow conditions (i.e., the Froude number, $\mathbb{F}$, is equal to 1). On this basis the peak flow can be calculated by solving for velocity in the Froude equation, and substituted into the continuity of mass equation for a simplified equation of discharge:

$$Q = A\sqrt{\frac{gA}{T_w}} \qquad \text{(Eq. 3)}$$

where A is the cross sectional area of the flow (m^2), T_w is the top width of the wetted area (m), and g is gravitational acceleration (9.81 m/s^2). In our analysis, the critical flow method used the same cross-sections as in the slope-area method.

3.3.4. HEC-RAS MODELING

One-dimensional hydraulic modeling is more complex than the at-a-station calculations described above, as it can account for nonuniform flow and downstream variation in mean fluid velocity and momentum. We used HEC-RAS 4.1.0 [*USACE*, 2010] to estimate the range of discharges and channel roughness for each flood. The model requires a series of cross-sections for input topography, and it then solves the one-dimensional energy equation to compute cross-sectionally averaged flow depth and velocity.

The longitudinal profile was created for each DEM using the built-in *Spatial Analyst Tools: Hydrology* within ArcGIS 10.1. The attribute tables were populated with the elevation and the coordinates for each inflection point along the thalweg. Cross-sections were hand digitized in ArcGIS perpendicular to the contours at an average spacing of ~28 m (Figure 5). HEC-GeoRAS 10.1 [*USACE*, 2011] was used to extract the longitudinal profile and cross-section elevations from each DEM. Because the LiDAR datasets were collected during summer/fall periods of very low or no flow in Skin Gulch, laser absorption by water was not a major concern, and cross-sections extracted from the LiDAR compare well with survey data (Figure 4).

We used HEC-RAS to compute the steady-state one-dimensional flow field for a suite of channel roughness and water discharge combinations. The goal was to find combinations of peak discharge and roughness that best matched observed high water marks, thereby bracketing the likely peak discharge for each flood. The Manning roughness coefficient was varied from 0.04 to 0.10 in increments of 0.02. Although roughness can vary spatially with depth, grain size, vegetation, channel obstructions, and bedforms, conducting simulations with uncertain distributions of how roughness varies spatially complicates the interpretation of model results. Additionally, because vegetation within the channel margins of SG was burned off by the fire, it is unlikely that roughness differed greatly between the channel and adjacent floodplains. Our 1D and 2D models therefore adopt a uniform roughness value for the entire modeled reach, and the effect of roughness variability may be inferred by comparing runs of different roughness. For each roughness value, we conducted simulations where water discharge inputs were varied from 70 to 240 m^3/s in 5 m^3/s increments for the 2012 flood and from 5 to 100 m^3/s in 5 m^3/s increments for the 2013 flood. A mixed flow regime was used, and the upstream and

downstream boundary conditions were set to normal flow where the slope was estimated from the bed topography.

RAS Mapper was used to create depth (.flt) files for each simulation and a Matlab script converted these files to ArcGRID ASCII files [*Perron*, 2013]. The resulting depth grid was added to the corresponding DEM to create a water surface profile that could be compared to the surveyed HWMs. The RMSE between the modeled water surface elevation and the measured HWMs was calculated for each simulation in order to determine a best estimate of n and Q. Each DEM provided a temporally explicit peak discharge estimate for each flood.

The 2012 flood was simulated with the 2012 NEON DEM, which was collected after the flood. Field observations suggest the flood produced mostly deposition in the study reach, and the 2012 NEON DEM reflects the cumulative deposition, and therefore calculations using this DEM likely underpredict the peak discharge. The 2013 flood was simulated using both pre- and post-flood LiDAR topography. A comparison of the peak discharge calculated for the 2013 storm using pre-flood and post-flood topography allows us to assess the effect that topographic changes have on post-event indirect discharge calculations.

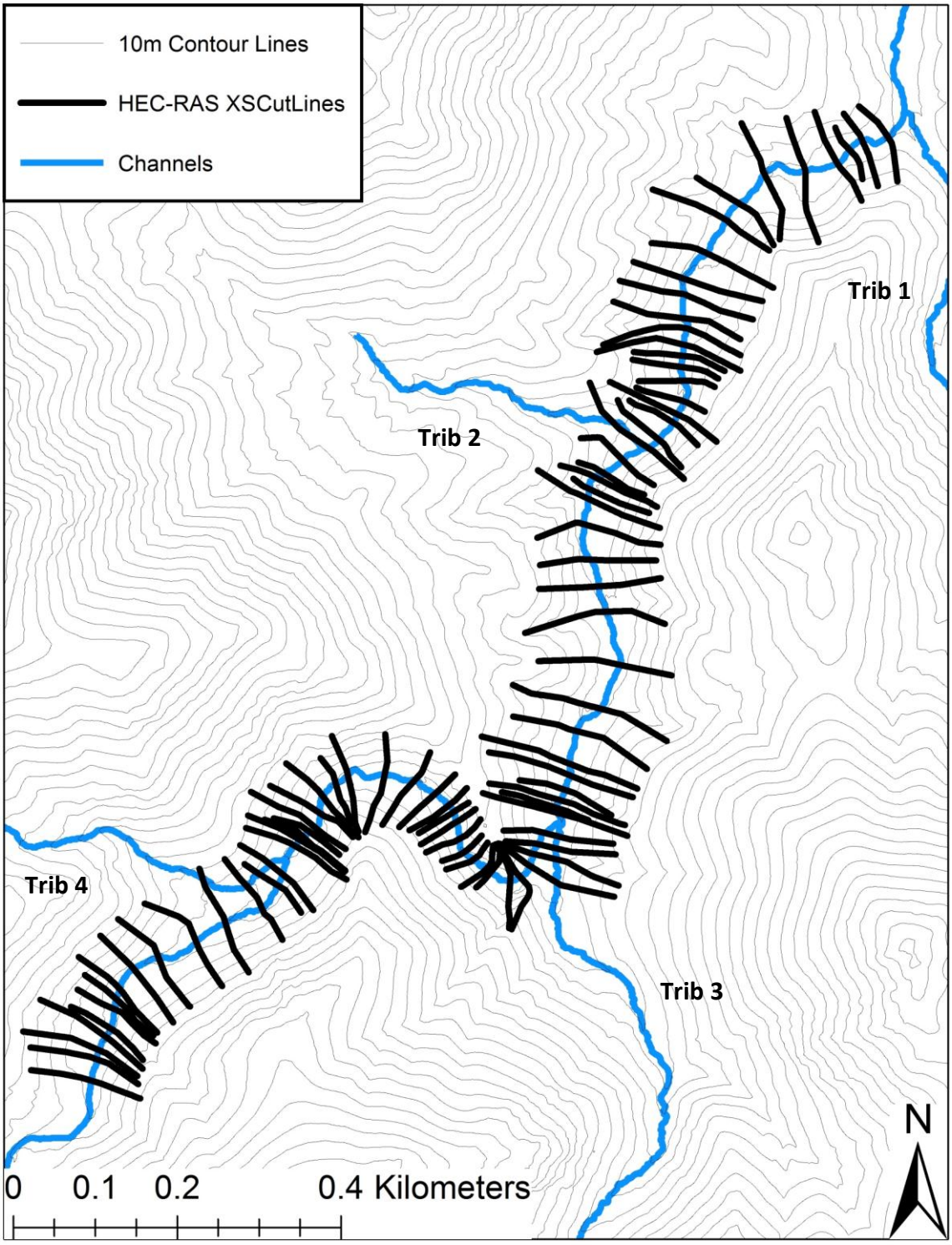

Figure 5. Cross-sections used in HEC-RAS modeling of the 2012 event.

3.3.5. TWO-DIMENSIONAL MODELING

Two-dimensional hydraulic modeling is capable of calculating cross stream variations in depth and velocity and potentially provides more useful information than one-dimensional or at-a-station calculations for forensic discharge analysis. We used Nays2D [e.g. *Asahi et al.*, 2013] to estimate the peak discharge for the 2012 and 2013 floods. Nays2D is a freely-available open-source model distributed with the International River Interface Cooperative (iRIC) software package. Nays2D solves the two-dimensional depth-averaged equations of fluid continuity and momentum to determine the water surface elevation and depth-averaged velocity. These equations are solved in a general curvilinear coordinate system, enabling computational meshes of any shape [*iRIC Software*, 2013].

As with the one-dimensional modeling, Nays2D was used to compute two-dimensional steady-state flow fields for varying combinations of peak discharges and channel roughness values. Sixty-seven discharge, Manning's roughness coefficient, and DEM combinations were modeled. Simulations were computed for spatially uniform Manning's roughness coefficients ranging from 0.04 to 0.10 in increments of 0.02, and for constant discharges of 60 to 150 m^3/s in 5 m^3/s increments for the 2012 flood and 5 to 60 m^3/s for the 2013 flood. Grid cells were 2 m x 1 m with the long axis oriented downstream. Upstream and downstream boundary conditions were set to uniform flow. The cubic-interpolated pseudoparticle method was used for finite differential calculation of the advection terms. The zero equation model was used for eddy viscosity parameterization:

$$v_t = \frac{k}{6} u_* h \qquad \text{(Eq. 4)}$$

where v_t is the eddy viscosity coefficient, k is the Karman coefficient (0.4), u_* is velocity (m/s), and h is depth (m).

Each simulation was run at a time step of 0.01 s using a relaxation coefficient for water surface calculations of 0.8 for a total of 1000 seconds, at which point it was verified that steady conditions had been reached. The primary model outputs for each simulation were the local depth (h) and the 2D depth-averaged velocity vectors (u, v). Boundary shear stress (τ_x, τ_y) in Nays2D is calculated with a drag coefficient closure:

$$(\tau_x, \tau_y) = \rho C_d \sqrt{u^2 + v^2}(u, v) \quad \text{(Eq. 5)}$$

where

$$C_d = \frac{gn^2}{h^{1/3}}. \quad \text{(Eq. 6)}$$

The RMSE was calculated between the model-computed water surface elevation and observed HWMs for each simulation.

Two-dimensional models can calculate superelevation of the water surface in bends, where centrifugal accelerations cause the water surface on the outer bank to be higher than the inner bank [e.g. Dietrich, 1987] and the magnitude of this superelevation depends on the flow velocity. One location in our 2012 survey had HWMs that were on opposing sides of the channel where the accuracy of the cross-stream water surface profile computed by the 2D model could be assessed. This superelevation provided an additional check on model performance and reduced the uncertainty in the Manning roughness coefficient and discharge values. Unfortunately this analysis was not possible for the 2013 flood as there were no clear HWMs on opposing sides of the channel.

4. RESULTS

4.1. PRECIPITATION

The bias corrections for each storm are usually greater than one, indicating that uncorrected NEXRAD radar tended to underestimate precipitation (Table 2). The western portion of lower Skin Gulch was subjected to high-intensity convective thunderstorms on 6-7 July 2012 that lasted ~20 hours, and had a maximum total depth of ~50 mm (Figure 6a). Much of the rain came in two 15-min bursts with a maximum 15-minute intensity of roughly 53 mm/h over areas of high burn severity (Figure 1, Figure 6b, and Figure 7a). The recurrence intervals for total storm depth and the maximum 15-minute intensity (Figure 6a and Figure 6b) were 1-2 and 2-5 years, respectively [*Perica et al.*, 2013].

Table 2. Daily mean field bias (MFB) for the radar data during the 2012 and 2013 floods.

Date	2012 MFB
6-Jul-12	0.211
7-Jul-12	0.951

Date	2013 MFB
9-Sep-13	0.84
10-Sep-13	1.61
11-Sep-13	5.48
12-Sep-13	4.96
13-Sep-13	5.87
14-Sep-13	6.00
15-Sep-13	2.39

In contrast to the 2012 storm, the September 2013 storm lasted roughly seven days. This storm produced about 280 mm of rain (Figure 6c), this value matches well with the data from hundreds of precipitation gage records throughout the Front Range [*Lukas et al.*, 2013]. The maximum 15-minute rainfall intensity compiled from bias-corrected radar was about 100 mm/h (Figure 6d, and Figure 7a), which is nearly three times the maximum 15-minute intensity of 38

mm/h that was measured by any recording rain gage. The recurrence interval of the 6-day total precipitation of 280 mm is estimated at 1000+ years [*Perica et al.*, 2013].

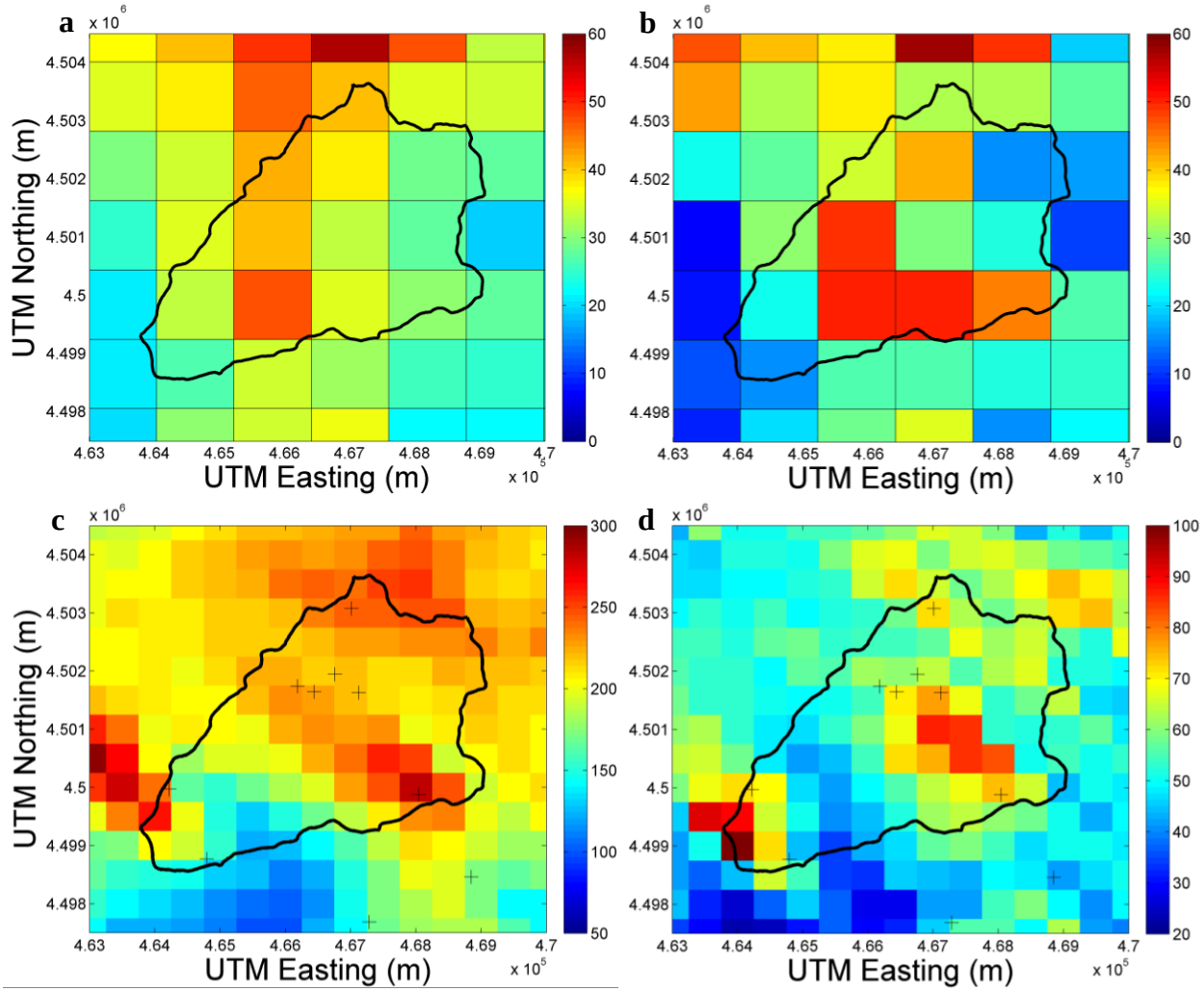

Figure 6: (a) Total precipitation in mm, and (b) maximum 15-min rainfall intensity estimates in mm/h for 6-7 July 2012 17:30 UTC to 7 July 2012 13:00 UTC using Hydro-NEXRAD. (c) Total precipitation in mm, and (d) maximum 15-min rainfall intensity estimates in mm/h for 9-15 September 2013 using DAA data. Crosses indicate locations of precipitation gages.

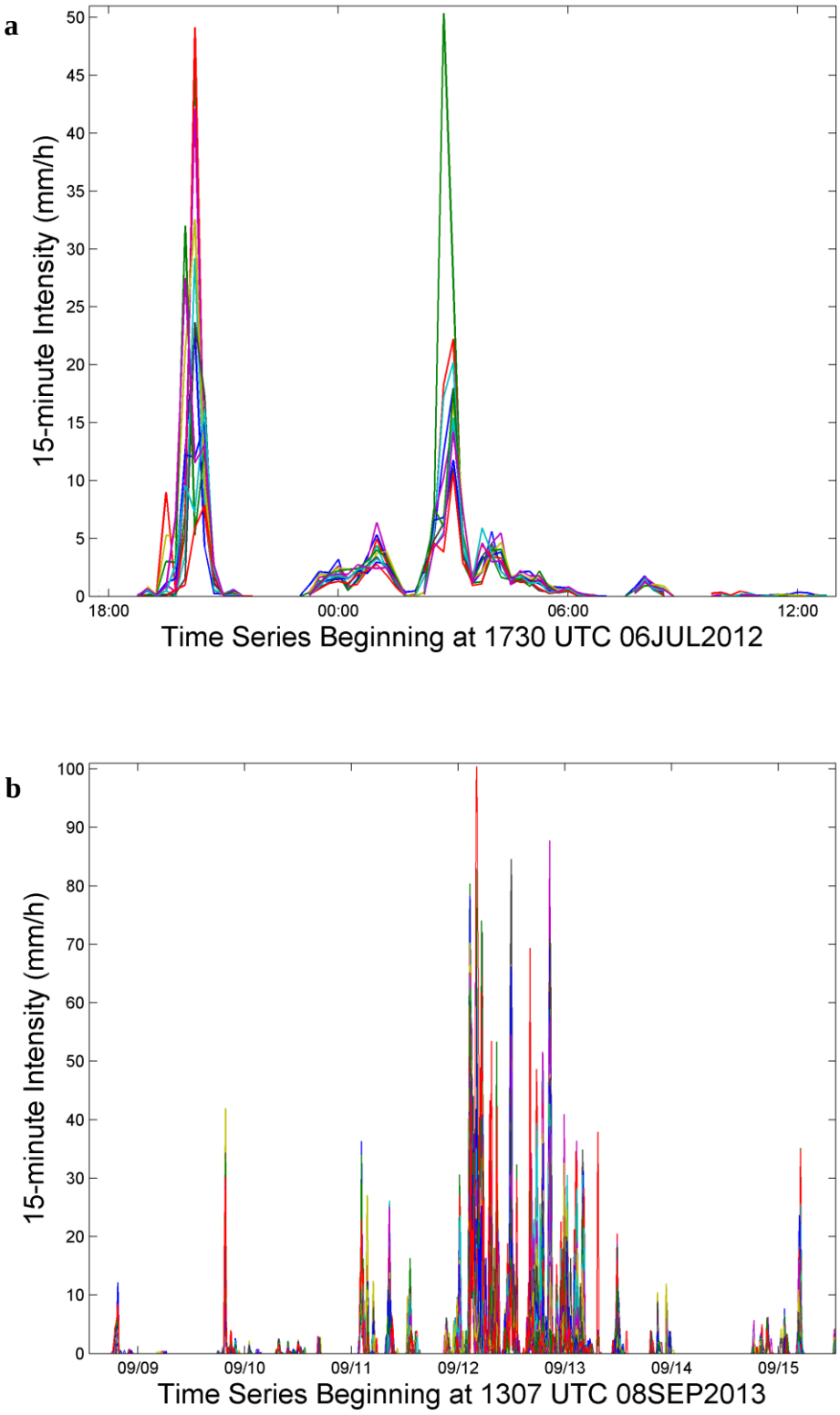

Figure 7. Bias-corrected 15-minute rainfall intensity for each radar pixel within SG for the (a) 2012 storm; and (b) the 2013 storm.

4.2. PEAK FLOWS

4.2.1. SLOPE-AREA METHOD

The slope-area method yielded peak discharges of 13.5 to 245 m^3/s for the July 2012 flood, and 0.9 to 66 m^3/s for the September 2013 flood (Figure 8; APPENDIX). The four-fold variation in *n* (0.03 – 0.12) used in these calculations resulted in a four-fold variation in the estimated discharges at a cross section. There also is considerable variability between cross-sections when roughness is held constant. For example, XS3, XS4, and XS5 are very close to each other (<140 m along the channel centerline), but the estimated discharge for the 2012 flood at XS5 is only about one-third of the estimated discharge at XS3 and XS4. The HWM located next to XS5 is on the inside of a channel bend and tucked into trees, which might help explain the lower discharge results compared to the other cross-sections. XS8 is ~630 m farther upstream, yet the estimated range of discharges for the 2012 flood is more than 40% greater than any of the other cross-sections. The decrease in discharge values in the downstream direction is likely due to flood attenuation and a loss of surface flow to subsurface flow when the valley width increases from a narrow ~20 m bedrock confined valley bottom to a wider ~40 m alluvial valley bottom.

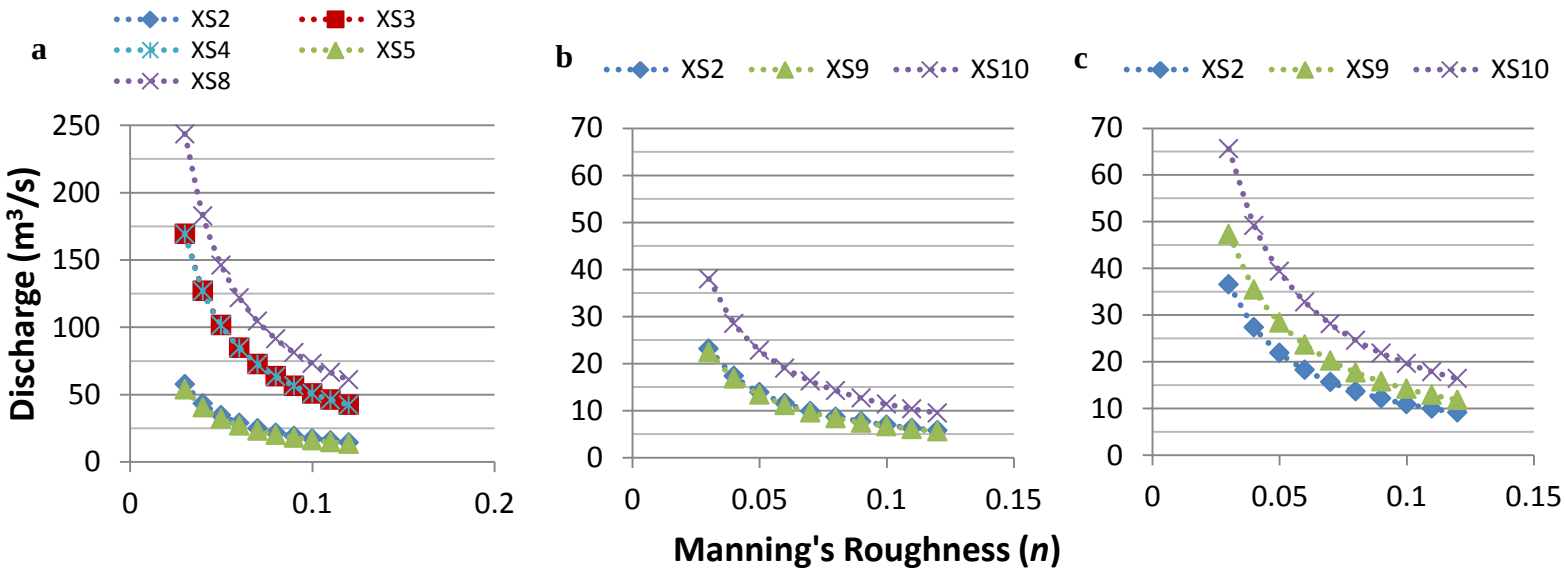

Figure 8. Decrease in predicted discharge with an increase in Manning's roughness coefficient for the slope-area method for: a) 2012 post-flood, b) 2013 pre-flood, and c) 2013 post-flood

The channel expansion located near XS6 explains the considerable LWD piled against trees (Figure 9a), and the boulder-sized clasts that were mobilized and imbricated between XS8 and XS9 (Figure 9b) during the 2012 flood. The largest imbricated boulder that we measured had an intermediate axis of 1080 mm, while the average diameter of the 60 imbricated boulders we measured was just over 300 mm. The observed deposition was not uniform across all channels (it was limited to the blue area in Figure 2); as the main channel to the west had dramatic geomorphic changes, while Tributaries 3 and 4 were largely unaffected by the storm.

a

b

Figure 9. (a) LWD pushed against standing tree near XS6, and (b) imbricated boulders above channel bed between XS8 and XS9.

During the first summer after the wildfire (i.e., July-September 2012) the channel appeared intermittent due to significant subsurface flow through the large amount of sediment deposited in the channel after the fire. By the summer of 2013, the channel became redefined through the deposited material and was flowing perennially. During the September 2013 flood, the channel substantially widened and incised, and the valley bottom was substantially reworked.

The discharge computed at XS10 is greater than that computed at XS9, even though the two sections are merely 400 m apart and includes flow contribution from tributary 4. Despite the uncertainty associated with the appropriate choice of roughness, survey data, and pre- vs. post-flood topography, the slope area method consistently calculated larger peak flow for the 2012 flood than for the 2013 flood.

The September 2013 flood produced a very erosional channel response, in that the channel primarily incised and widened resulting in undercuts, bank failures, and shallow landslides (Figure 10). Ultra-sonic depth measurements indicate the primary period of high flows lasted for 61.8 hours starting around 0045 UTC on 12 September 2013. The pre- and post-flood survey data show that the geomorphic response varied in the downstream direction (Figure 11). XS8 (Figure 11a) experienced ~1.7 m of incision, while at XS4 (Figure 11b) the active channel width increased from ~3 m to ~23 m and the thalweg only incised by ~0.3 m. This increase in cross-sectional area is why the slope-area method yielded higher values for the post-2013 flood than the pre-2013 flood (Figure 10 and Figure 11; APPENDIX).

a

b

Figure 10. Photos looking downstream at XS4, with (a) being prior to the September 2013 flood, and (b) the same location after the flood. Note the same tree in the upper left of both pictures and the slope failure along the hillslope to the right.

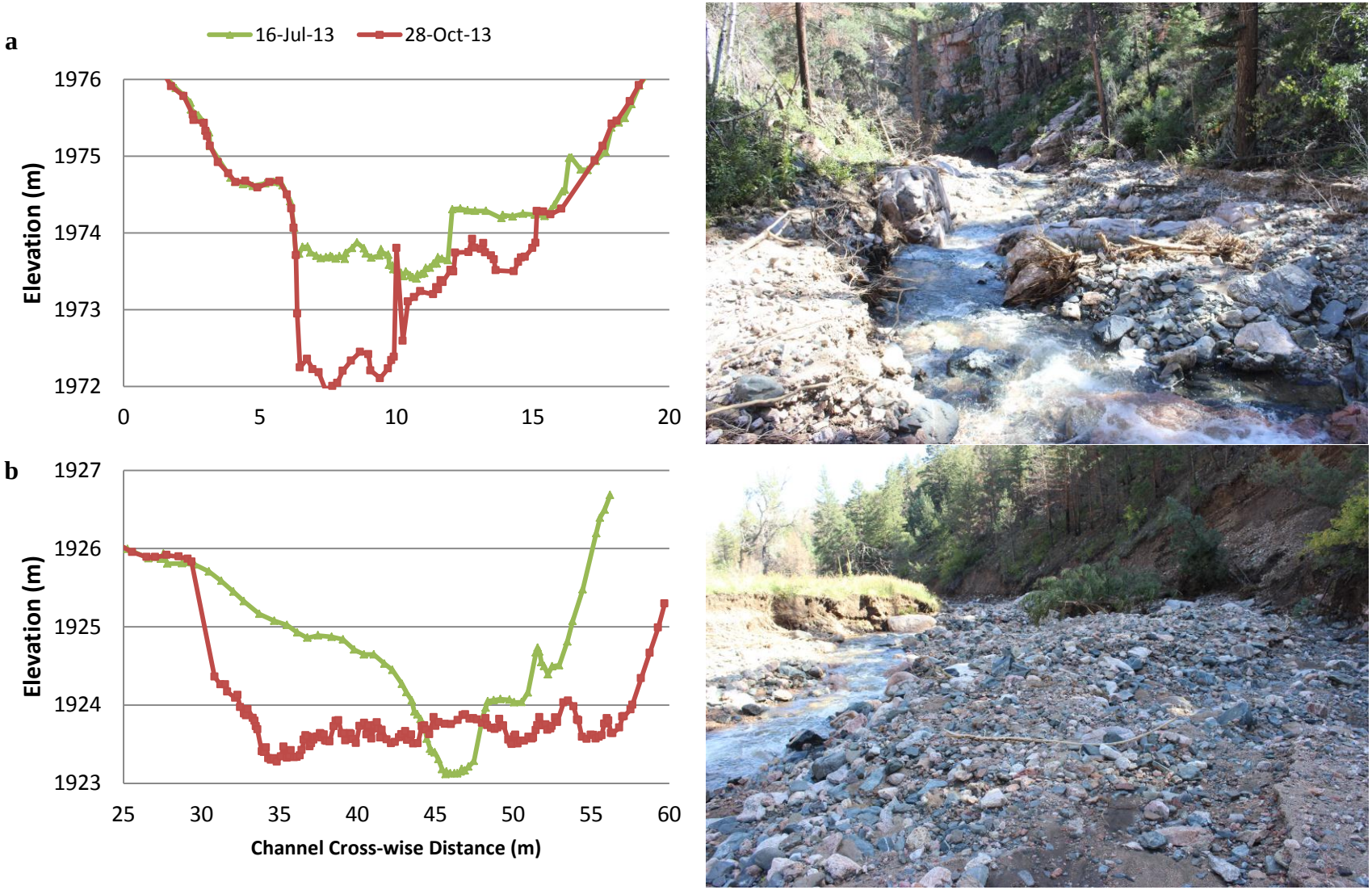

Figure 11. Pre- and post-2013 flood cross-section elevation comparisons and photos looking downstream for (a) XS8, and (b) XS4. Note the general trend of incision, and incision plus widening in the downstream direction. Photos taken on 24 September 2013.

4.2.2. CRITICAL FLOW METHOD

The peak discharge for the 2012 flood estimated with the critical flow method ranged from 37 – 112 m^3/s (Table 3) with an average value of 76 m^3/s. Peak discharge for the 2013 flood calculated with pre-flood topography averaged 21 m^3/s, while the 2013 peak discharge calculated using the post-flood topography averaged 34 m^3/s. These averages include estimates from cross sections where the HWM was located on an inner bend, which may underestimate the true water surface elevation due to centrifugal accelerations experienced by the flow. These data indicate that the 2012 flood was 2.8 – 4.6 times larger than the 2013 flood with a decreasing trend in discharge in the downstream direction.

Table 3. Critical flow results presented in m^3/s for the 2012 survey data, and the 2013 before and after September flood survey data

Cross-section	2012 post-flood topography m^3/s (ft^3/s)	2013 pre-flood topography m^3/s (ft^3/s)	2013 post flood topography m^3/s (ft^3/s)
XS2	52 (1840)*	16 (570)	23 (810)
XS3	97 (3430)	-	-
XS4	112 (3960)	-	-
XS5	37 (1310)*	-	-
XS8	82 (2900)	-	-
XS9	-	16 (570)	34 (1200)
XS10	-	31 (1100)	47 (1660)

*HWMs used include an inner bend HWM location

4.2.3. HEC-RAS MODELING

The peak flows for the 2012 flood computed using HEC-RAS that had the lowest RMSE ranged from 145 – 235 m^3/s for $n > 0.04$ (Figure 12; APPENDIX). The HEC-RAS estimates of peak flows for the 2013 flood with the lowest RMSE values vary from 20 – 45 m^3/s using pre-flood topography and from 40 – 90 m^3/s using post-flood topography. These values again indicate that the 2012 flood had a higher peak discharge than the 2013 flood, and that peak flow

estimates using 2013 post-flood topography yielded higher discharges than those using the pre-flood topography.

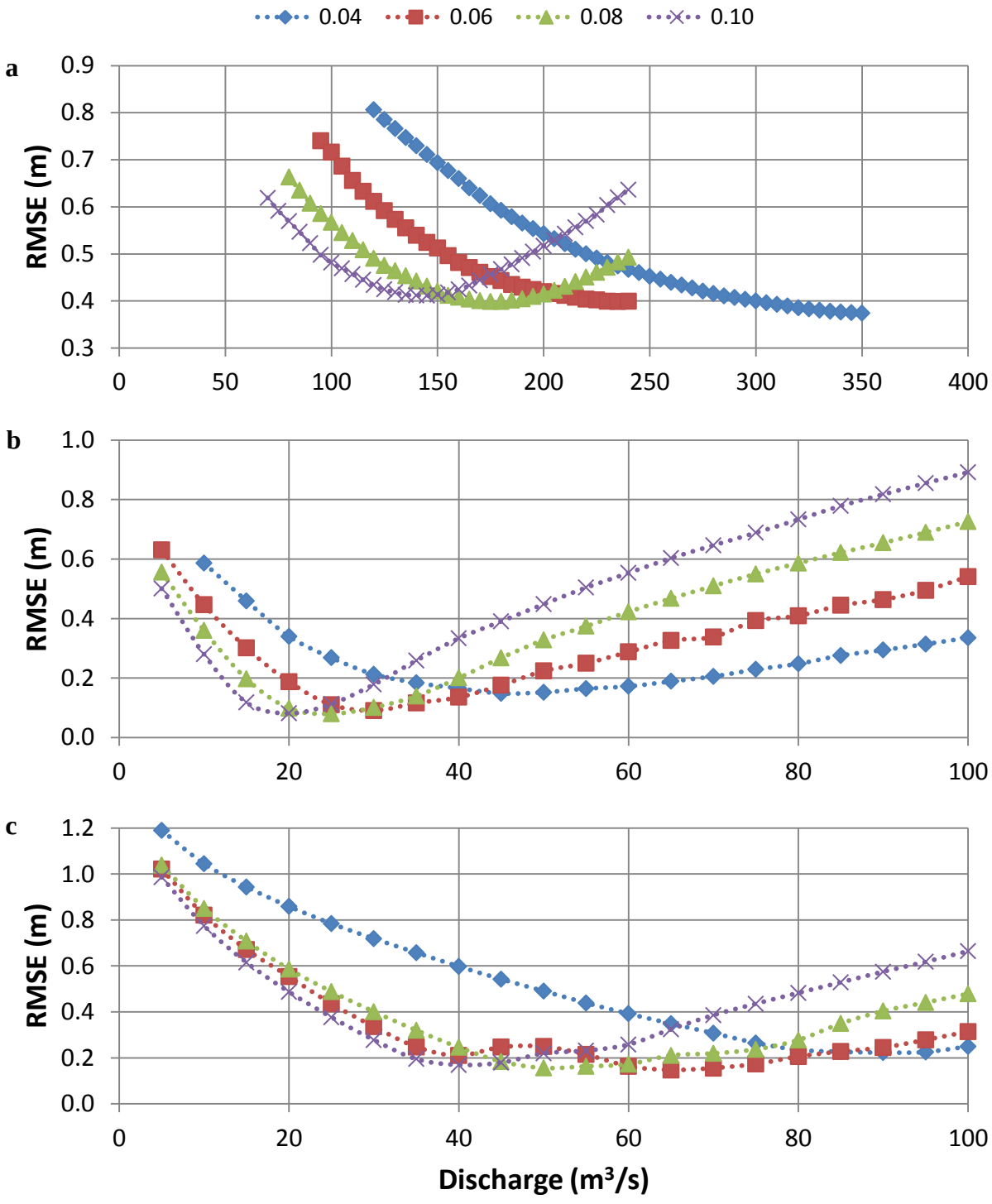

Figure 12. Graphs illustrating the RMSE from HEC-RAS for combinations of *Q* and *n* for: a) 2012 NEON, b) 2013 NEON, and 3) 2013 FEMA. The best discharge estimate for a given roughness value is that which minimizes the RMSE.

4.2.4. NAYS2D MODELING

The peak discharge with the lowest RMSE value computed with Nays2D for the 2012 flood ranged from 70 to 120 m^3/s depending on the roughness value (Figure 13a). The peak discharge with the lowest RMSE value for the 2013 event ranged from 5 to 20 m^3/s using pre-flood topography and 20 to 50 m^3/s using post-flood topography (Figure 13b and Figure 13c). These results are more constrained than the HEC-RAS results.

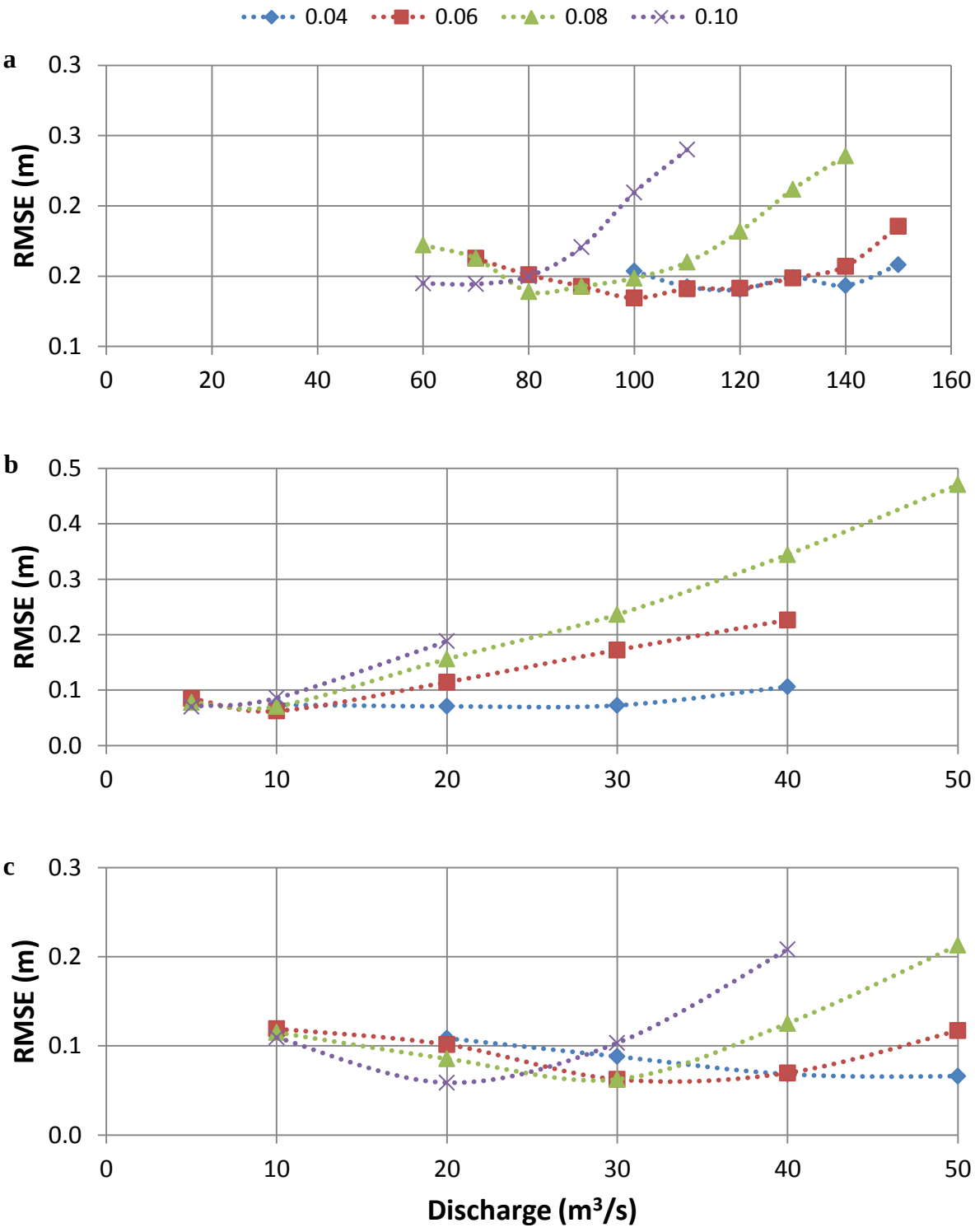

Figure 13. Graphs illustrating the RMSE from Nays2D for combinations of *Q* and *n* for: a) 2012 NEON, b) 2013 NEON, and 3) 2013 FEMA.

Observed superelevation of HWMs for the 2012 flood just downstream of XS6 had a difference in elevation of 0.55 m (Figure 14). The best 2D model had a superelevation of 0.56 m using n=0.10 and an estimated discharge of Q=70 m^3/s.

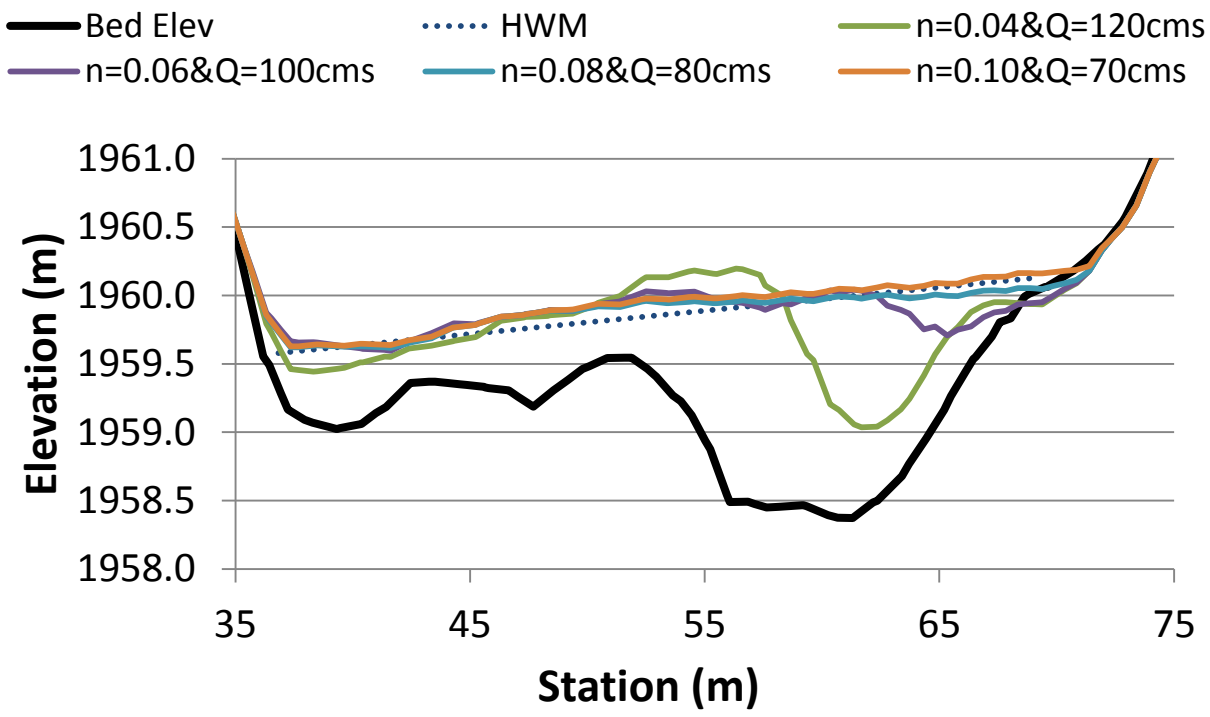

Figure 14. Example superelevation water surface profile for the 2012 flood. Note the vertical exaggeration of the y-axis.

Shear stress from the 2D model was mapped in order to identify areas of potential erosion and deposition (Figure 15). Constrictions and expansions strongly influenced the patterns of shear stress, with the largest stresses occurring in sharp constrictions. For the 2012 simulations, the spatial patterns of boundary shear stress were qualitatively compared with field observations of the locations of imbricated boulders and large woody debris (LWD) accumulations. The shear stress in the center of the channel is generally greater than 1000 Pa, which is competent to mobilize large 1-meter boulders [*Julien*, 2010] including the imbricated particles we measured.

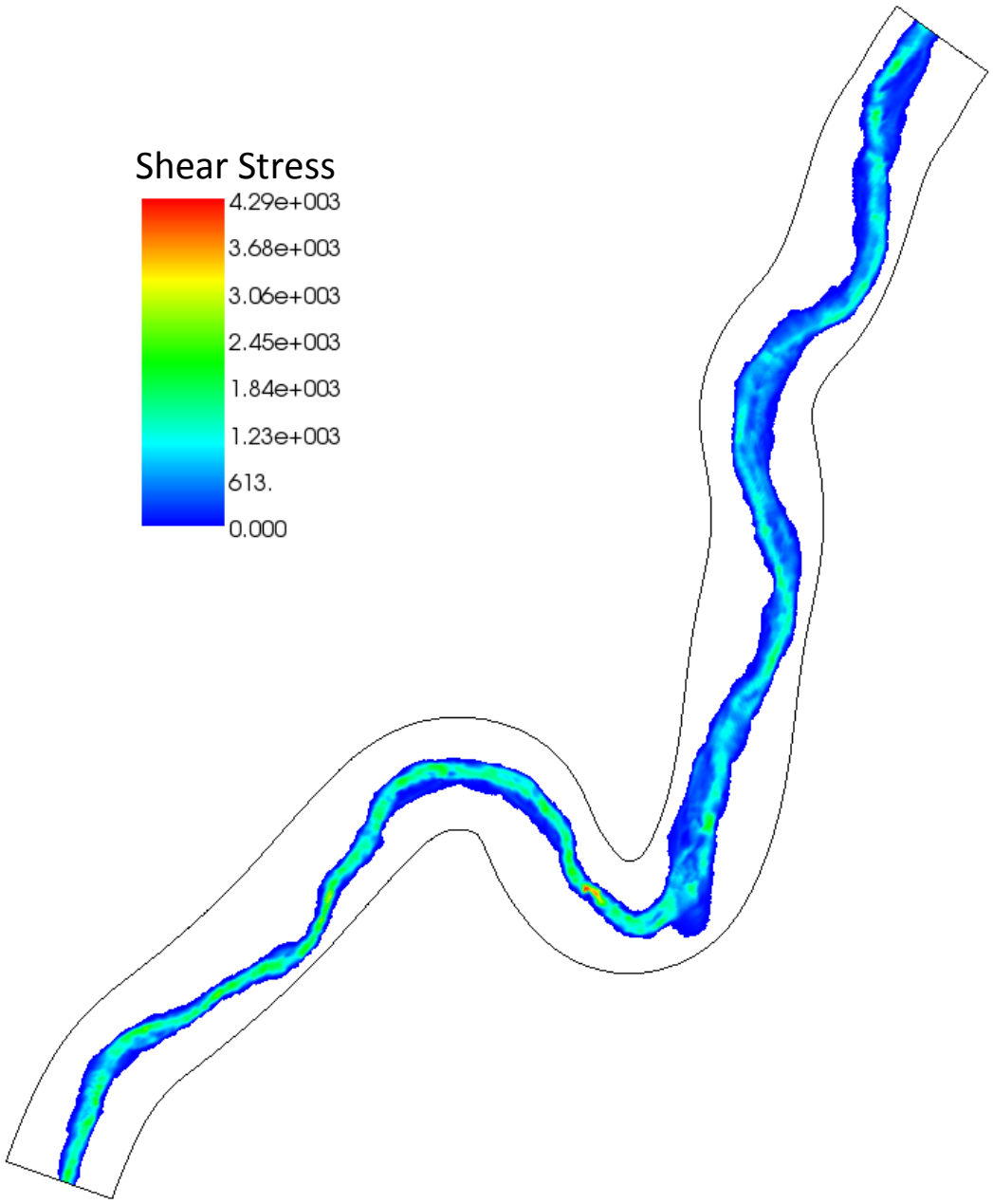

Figure 15. Patterns of shear stress in Pa for the 2012 flood Nays2D model using a combination of *n*=0.10 and *Q*=70 m^3/s.

4.3. SUMMARY OF PEAK FLOW CALCULATIONS

The various methods of peak discharge analysis provide a wide range of possible discharges and roughness characteristics for the July 2012 and September 2013 flood (Table 4).

The slope-area method depends heavily on the roughness and therefore the best estimate is challenging to determine. The critical flow method yielded a likely discharge of ~76 m^3/s for the 2012 flood and a range of 21 – 34 m^3/s for the 2013 flood. Peak discharges calculated for the critical flow method with post-flood 2013 topography are about 1.5 to 3 times larger than those calculated with pre-flood topography, illustrating the uncertainty in making flow calculations with survey data collected before and after a channel altering flood (Figure 11). HEC-RAS results suggest the 2012 flood was at least 145 m^3/s and potentially could have exceeded 350 m^3/s. The 2013 HEC-RAS results provide a range of discharges between 20 – 90 m^3/s. The best 2D model results estimated the 2012 peak discharge at 70 m^3/s with a Manning's roughness coefficient of 0.10. The 2013 analysis had more uncertainty due to the lack of any superelevation data, and range of discharges was between 5 and 20 m^3/s using pre-flood topography and 20 to 50 m^3/s using post-flood topography.

Table 4. Summary table of peak discharge values

Method	2012 post-flood topography m^3/s	2013 pre-flood topography m^3/s	2013 post-flood topography m^3/s
Critical flow	97	21	34
HEC-RAS	145 – 350+	20 - 45	40 - 90
Nays2D	70	5- 20	20 - 50

5. DISCUSSION

5.1. RECREATING EXTREME FLOODS

The wide range of discharge results from the four hydraulic analysis methods demonstrates the difficulty in accurately estimating floods with no direct discharge measurements and an evolving channel bed. The uncertainty in Manning's roughness coefficient has the greatest impact on the at-a-station slope-area method because the calculated discharge is linearly related to the roughness coefficient. Roughness had a similar influence on the HEC-RAS calculations; for example, the lowest RMSE discharge for the 2013 storm using pre-flood topography and n = 0.04 was 45 m^3/s, while the predicted discharge with n = 0.08 was 25 m^3/s. The Nays2D results were less sensitive to roughness; for the 2012 storm, a doubling of n from 0.04 to 0.08 resulted in only a 33% decrease in the best-fit discharge (from 120 m^3/s to 80 m^3/s). The roughness often can be constrained to a more narrow range by field observations [e.g. *Barnes*, 1967; *Acrement & Schneider*, 1989] or channel topography [e.g. *Limerinos*, 1970; *Jarrett*, 1985], but there will still be considerable uncertainty in n. *Wohl* [1998] suggested that roughness uncertainty typically introduces errors of up to 20% for paleohydrologic studies using step-backwater modeling.

The critical flow method does not require a roughness estimate, but assumes that the Froude number is equal to 1. Several studies have shown that the critical flow method works well for paleohydrology [e.g. *Grant*, 1997; *Webb & Jarrett*, 2002]; however, for large floods in steep channels, the Froude number can greatly exceed 1.0 [*Costa*, 1987]. A map of the estimated Froude numbers for the 2013 flood using the 2D model shows that the majority of the active channel has a Froude number between 0.8 – 1.2 (Figure 16). Peak discharges will be

overestimated at the margins of the channel where $\mathbb{F} < 0.8$, and underestimated along the center of the channel where $\mathbb{F} > 1.2$. This suggests that the critical flow method may considerably under- or over-estimate peak discharges for large floods in steep catchments depending on the location of the cross-section used in the analysis.

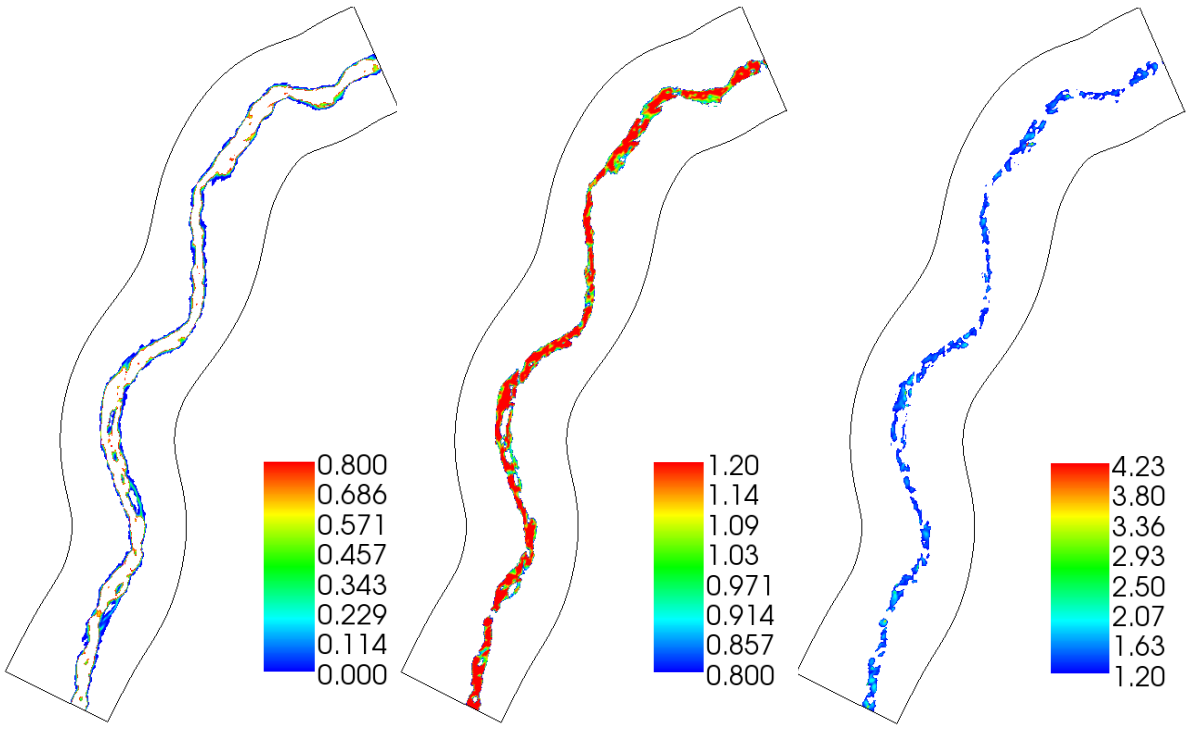

Figure 16. Location of Froude numbers below 0.8, from 0.8 to 1.2, and greater than 1.2 for the 2013 post-flood topography analysis for the Nays2D combination of n=0.06 and Q=30 m^3/s.

For a given roughness, the discharges computed by HEC-RAS that best fit the observed HWMs were consistently higher than the best-fit discharges computed with Nays2D (Table 4). This outcome is similar to the findings from *Alho & Aaltonen* [2008], who showed that HEC-RAS simulations of glacial outburst floods consistently predicted a smaller flood inundation area for a given hydrograph than a two-dimensional finite element model (TELEMAC-2D). These differences are due in part to the way HEC-RAS must parameterize processes that are readily computed in a 2D model, such as energy dissipation from small-scale variations in channel

width, expansions and constrictions, flow separation and eddy losses, and sinuosity at a scale less than the HEC-RAS cross-sections.

The 2D calculations had the lowest range of variability of the best estimates as compared to the HEC-RAS results. The capability of matching field observations of superelevation with 2D models further reduces uncertainty due to the roughness parameter. This suggests that, when possible, two-dimensional modeling is preferable for indirect discharge calculations.

Simulations of the 2013 event using pre- and post-flood topography show that much of the uncertainty in the calculation is due to the unknown timing of bed elevation changes. For example, assuming $n = 0.08$, the discharge for the optimal RMSE value was 10 m^3/s for pre-2013 flood and post-2013 flood the discharge was estimated to be 30 m^3/s or three times larger. In contrast, the discharge varies from 20 – 50 m^3/s when maintaining the same 2013 post-flood DEM, which only varies by 2.5 across the entire range of roughness values. This intra-event uncertainty in bed topography, along with uncertainties inherent to topographic data collection in general (such as survey or LiDAR instrumentation accuracy, topographic point spacing, or DEM resolution), suggest that in some cases model predictions are better represented as probabilistic distributions rather than specific values (e.g. *Legleiter et al.*, 2011). The true peak discharge for the 2013 flood should lie between the values calculated with pre- and post-flood topography, while the deposition associated with the 2012 storm means that our estimated peak flows using post-flood topography are probably too low. 1D and 2D morphodynamic models that simulate sediment transport and bed evolution along with flood hydrodynamics would provide a useful avenue for future research in indirect discharge measurements and paleohydraulic studies.

5.2. COMPARISON OF THE 2012 AND 2013 EVENTS

The 2012 event in SG was exceptional, as it falls between the 90th and 99th percentile curves of the largest rainfall-runoff floods per unit area recorded in the United States (Figure 17; [*Costa and O'Connor*, 1995]). This event is even more unusual for a rainfall-runoff flood in a semi-arid or snowmelt-dominated region like the Rocky Mountains (Figure 17, inset). The high intensity, short-duration rainfall (Figure 6b and Figure 6c) over areas of high burn severity in the upper portions of Skin Gulch (Figure 1 and Figure 6a) produced a historically large flood from a summer thunderstorm with a recurrence interval on the order of one to five years. The extreme magnitude of the estimated peak flows for the 2012 flood indicates the importance of the change in runoff processes after a high-severity fire.

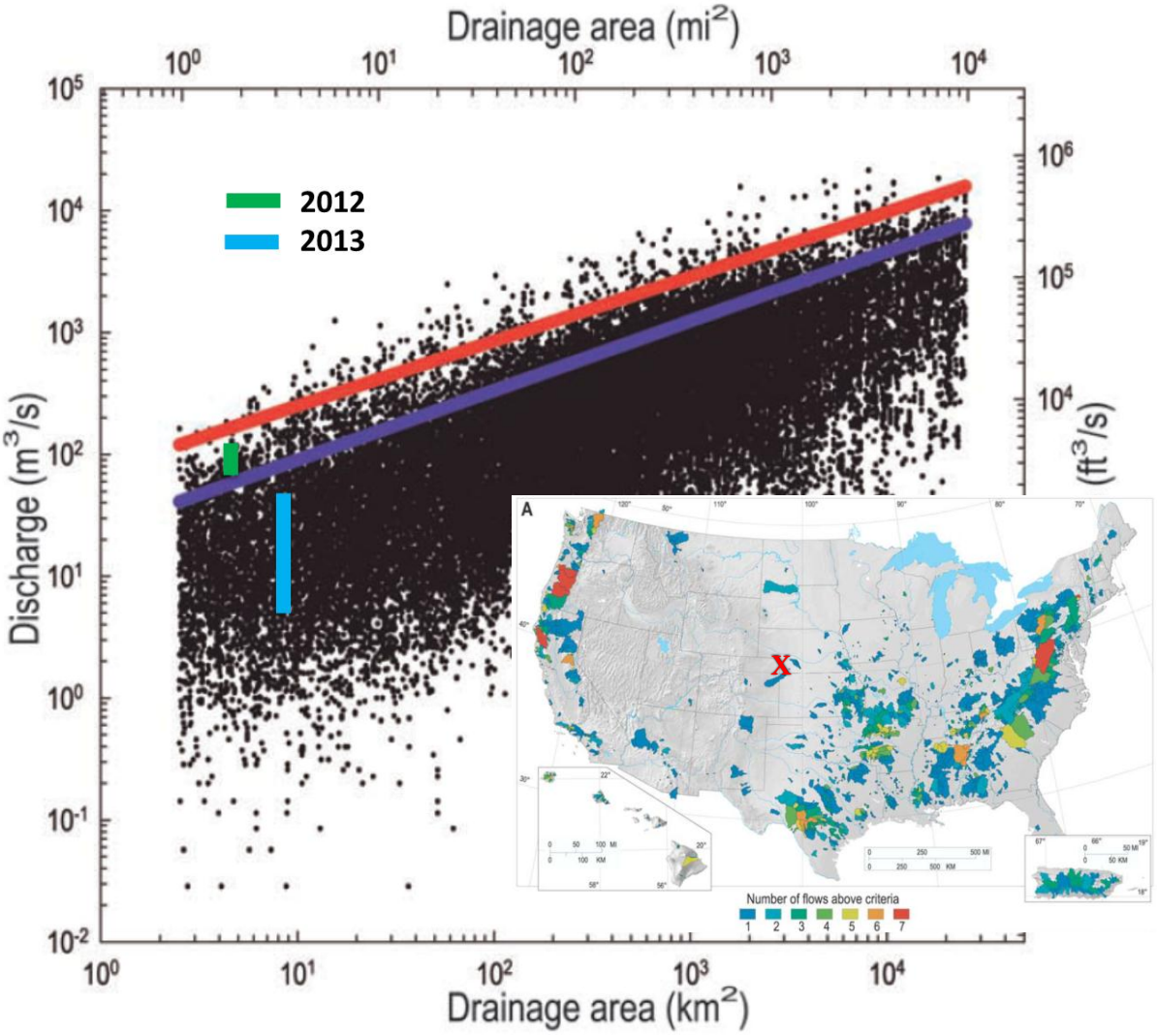

Figure 17. Range of peak discharges with the lowest RMSE values from Nays2D for the 2012 and 2013 flood events in SG plotted with the largest rainfall-runoff floods experienced in the United States and Puerto Rico [modified from *O'Connor & Costa*, 2004]. The blue and red lines correspond to the ~90th and ~99th percentiles. Inset map [from O'Connor and Costa, 2004] shows the locations of watersheds contributing to the plot, and the red X indicates the location of SG.

Recently burned areas have higher rates of infiltration-excess runoff [*Onda et al.*, 2008; *Ebel et al.*, 2012] due to the reduced ground and surface cover, increased soil water repellency, and soil sealing [*Debano*, 1981; *DeBano*, 2000; *Huffman et al.*, 2001; *Larsen et al.*, 2009; *Moody et al.*, 2008; *Neary et al.*, 1999; *Pietraszek*, 2006]. The higher rates of runoff, readily available sediment on the hillslopes and along the channel, and the depositional nature of the 2012 flood suggest that the flood response was sediment transport capacity-limited. The 2013 flood was

sediment supply-limited as evident by the erosional nature of the flood. The hydrologic effects of wildfire tend to be temporary, as post-wildfire runoff and erosion rates decrease significantly within three years [*Morris & Moses*, 1987; *Robichaud et al.*, 2000; *MacDonald & Larsen*, 2009]. The lower peak discharge of the 2013 flood compared to the 2012 flood is partially due to this recovery; however, differences in precipitation intensity probably also played an important role. Although the maximum 15-minute rainfall intensity estimated by the radar for the 2013 storm tended twice than the peak rainfall intensities of the 2012 storm (Figure 7), the 2013 radar-estimated intensities are around three times higher than the maximum 15-minute intensity recorded by the rain gages. If, as the rain gage data suggest, the highest 15-minute intensity over the 2013 storm was 38 mm/h, then it is reasonable to expect the peak discharge for that flood to be lower than that of the 2012 flood, even though the storm lasted for six days. Although applying a daily MFB has been shown to be better than applying no bias at all [*Smith et al.* 2005; *Wright et al.* 2013], the results suggest that using radar to estimate short-term rainfall intensities for spatially extensive, multi-day storms in the mountains remains challenging.

Both storms produced considerable geomorphic change (Figure 9 – Figure 11); however, all of our hydraulic calculations suggest the peak discharge of the 2013 flood was much smaller than that of the 2012 flood (Table 4). While the changes resulting from the 2012 storm were due to the exceptionally high peak discharge it produced, the geomorphic changes from the 2013 storm were likely a consequence of the much longer duration of flooding. The energy available for geomorphic change is the time integral of the unit stream power above an alluvial erosion threshold [*Costa and O'Connor,* 1995]; and the 2013 flood lasted for 62.8 hours. The long duration, and seemingly large total energy expenditure was significant enough to rework the channel and cause substantial erosion.

Major geomorphic events like these lead to legacy features that affect the long-term evolution of the landscape [*Roering & Gerber*, 2005]. Several of the large boulders that were mobilized by the 2012 event and bedrock exposed by the 2013 event will likely persist for many decades to centuries [e.g. *Meyer et al.*, 1992; *Meyer et al.*, 1995; *Moody & Martin*, 2001a; *Legleiter et al.*, 2003]. The fire and flooding sequence in SG may constitute a "millennium scale" aggradational event [*Elliott and Parker*, 2001] in which severe, watershed-scale forest fire and subsequent extreme flooding cause an aggradational signature that persists for centuries. Future work in SG will include radiocarbon dating of fire layer stratigraphy to more fully link the cycle of fires and floods in this environment.

6. CONCLUSIONS

The July 2012 and September 2013 storms and associated floods in SG provide insight on the influence of wildfire on extreme floods and geomorphic evolution. Although the July 2012 thunderstorm had relatively modest storm total precipitation and 15-minute intensity, the resulting flood caused tremendous channel change, was capable of transporting boulders, and ranks among the largest rainfall-runoff floods per unit area ever recorded in the United States. The magnitude of this event shows how the coincidence of a recent, high severity burn with locally intense rainfall can produce truly exceptional hydrologic response and geomorphic changes. Total rainfall for the September 2013 storm was six times the rainfall for the 2012 thunderstorm, but the estimated peak discharge was much smaller than the 2012 event. The 2013 flood still caused significant channel changes, however, suggesting that the duration of relatively high flows had an important influence on the geomorphic effectiveness of the flood.

7. REFERENCES

Abbott, J. T. (1970). Geology of precambrian rocks and isotope geochemistry of shear zones in the Big Narrows Area, northern Front Range, Colorado. *United States Geological Survey, Denver, CO, Open-File Report 70-1*, 1–239.

Acrement, G. J. J., & Schneider, V. R. (1989). Guide for selecting Manning's roughness coefficients for natural channels and flood plains. *United States Geological Survey Water-Supply Paper 2339. Geological Survey Water-Supply Paper 1898-B.*

Alho, P., & Aaltonen, J. (2008). Comparing a 1D hydraulic model with a 2D hydraulic model for the simulation of extreme glacial outburst floods. *Hydrological Processes*, *22*, 1537–1547.

Asahi, K., Shimizu, Y., Nelson, J., & Parker, G. (2013). Numerical simulation of river meandering with self-evolving banks. *Journal of Geophysical Research: Earth Surface*, *118*, 1–22.

Baker, V., & Costa, J. (1987). Flood power. In L. Mayer & D. Nash (Eds.), *Catastrophic Flooding.* 1–21. Allen and Unwin, St. Leonards, N.S. W., Australia.

Barnes, H. H. J. (1967). Roughness characteristics of natural channels. Washington: U.S. Geological Survey Water-Supply Paper 1849.

Benavides-Solorio, J. D. D., & MacDonald, L. H. (2005). Measurement and prediction of post-fire erosion at the hillslope scale, Colorado Front Range. *International Journal of Wildland Fire*, *14*(4), 1–18.

Benavides-Solorio, J., & MacDonald, L. H. (2001). Post-fire runoff and erosion from simulated rainfall on small plots, Colorado Front Range. *Hydrological Processes*, *15*(15), 2931–2952.

Benda, L. E., Miller, D., Bigelow, P., & Andras, K. (2003). Effects of post-wildfire erosion on channel environments, Boise River, Idaho. *Forest Ecology and Management*, *178*(1-2), 105–119.

Borga, M., Gaume, E., Creutin, J. D., & Marchi, L. (2008). Surveying flash floods: gauging the ungauged extremes. *Hydrological Processes*.

Bowman, D. M. J. S., Balch, J. K., Artaxo, P., Bond, W. J., Carlson, J. M., Cochrane, M. A., D'Antonio, C. M., DeFries, R. S., Doyle, J. C., Harrison, S. P., Johnston, F. H., Keeley, J. E., Krawchuk, M. A., Kull, C. A., Marston, J. B., Moritz, M. A., Prentice, I. C., Roos, C. I., Scott, A. C., Swetnam, T. W., van der Werf, G. R., and Pyne, S. J. (2009). Fire in the Earth system. *Science*, *324*, 481–484.

Burton, T. A. (2005). Fish and stream habitat risks from uncharacteristic wildfire: Observations from 17 years of fire-related disturbances on the Boise National Forest, Idaho. *Forest Ecology and Management, 211*(1-2), 140–149.

Church, M. (2002). Geomorphic thresholds in riverine landscapes. *Freshwater Biology*, *47*(4), 541–557.

Cifelli, R., Doesken, N., Kennedy, P., Carey, L. D., Rutledge, S. a., Gimmestad, C., & Depue, T. (2005). The Community Collaborative Rain, Hail, and Snow Network: Informal education for scientists and citizens. *Bulletin of the American Meteorological Society*, *86*(8), 1069–1077.

Cook, A., & Merwade, V. (2009). Effect of topographic data, geometric configuration and modeling approach on flood inundation mapping. *Journal of Hydrology*, *377*, 131–142.

Costa, J. E. (1987). Hydraulics and basin morphometry of the largest flash floods in the conterminous United States. *Journal of Hydrology*, *93*, 313–338.

Costa, J. E., & O'Connor, J. E. (1995). Geomorphically effective floods. In *Natural and Anthropogenic Influences in Fluvial Geomorphology, Geophysical Monograph 89*. 45–56. AGU, Washington, D.C.

Debano, L. F. (1981). Water repellent soils: a state-of-the-art. *USDA Forest Service, Pacific Southwest Forest and Range Experiment Station, Berkeley, CA. General Technical Report PSW-46*.

DeBano, L. F. (2000). The role of fire and soil heating on water repellency in wildland environments: a review. *Journal of Hydrology*, *231-232*, 195–206.

DeBano, L. F., Ffolliott, P. F., & Baker Jr., M. B. (1996). Fire severity effects on water resources. In P. F. Ffolliott, L. F. DeBano, M. B. Baker Jr., G. J. Gottfried, G. Solis-Garza, C. B. Edminster, D. G. Neary, and R. H. Hamre (Eds.), *Effects of Fire on Madrean Province Ecosystems: a symposium proceedings.* 77–87. General Technical Report RM-GTR-289. Fort Collins, CO: USDA. Forest Service, Rocky Mountain Forest and Range Experiment Station.

Dietrich, W. E. (1987). Mechanics of flow and sediment transport in meander bends. In K. S. Richards (Ed.), *River Channels: Environment and Process.* 179–227. Oxford, UK: Basil Blackwell, Inc.

Dingman, S. L., & Sharma, K. P. (1997). Statistical development and validation of discharge equations for natural channels. *Journal of Hydrology*, *199* (1-2), 13–35.

Dunham, J. B., Young, M. K., Gresswell, R. E., & Rieman, B. E. (2003). Effects of fire on fish populations: landscape perspectives on persistence of native fishes and nonnative fish invasions. *Forest Ecology and Management*, *178*(1-2), 183–196.

Ebel, B. A., Moody, J. A., & Martin, D. A. (2012). Hydrologic conditions controlling runoff generation immediately after wildfire. *Water Resources Research*, *48*(3), 1–13.

Elliott, J. G., & Parker, R. S. (2001). Developing a post-fire flood chronology and recurrence probability from alluvial stratigraphy in the Buffalo Creek watershed, Colorado, USA. *Hydrological Processes*, *15*, 3039–3051.

Fulton, R. A., Breidenbach, J. P., Seo, D.-J., Miller, D. A., & O'Bannon, T. (1998). The WSR-88D Rainfall Algorithm. *Weather Forecast*, *13*, 377–395.

Gerbremichael, M., & Krajewski, W. F. (2004). Assessment of the Statistical Characterization of Small-Scale Rainfall Variability from Radar: Analysis of TRMM Ground Validation Datasets. *Journal of Applied Meteorology*, *43*, 1180–1199.

Grant, E. (1997). Critical flow constrains flow hydraulics in mobile-bed streams: A new hypothesis. *Water Resources Research*, *33*(2), 349–358.

High Park Fire Burned Area Emergency Response (BAER) Report. (2012). Department of Transportation, Larimer County, Natural Reserouces Conservation Service, U.S. Forest Service.

Huffman, E. L., MacDonald, L. H., & Stednick, J. D. (2001). Strength and persistence of fire-induced soil hydrophobicity under ponderosa and lodgepole pine, Colorado Front Range. *Hydrological Processes*, *15*(15), 2877–2892.

iRIC Software. (2013). Nays2D Solver Manual. 50 pp. Retrieved October 3, 2013, from http://i-ric.org/en/software/1.

Jarrett, R. D. (1985). Hydraulics of high-gradient streams. *Journal of Hydraulic Engineering*, *110*(11), 1519–1539.

Jarrett, R. D., & Costa, J. E. (1988). Evaluation of the flood hydrology in the Colorado Front Range using precipitation, streamflow, and paleoflood data for the Big Thompson River Basin. *United States Geological Survey, Denver, CO. Water-Resources Investigations Report 87-4117*.

Jin, S., Yang, L., Danielson, P., Homer, C., Fry, J., and Xian, G. (2013). A comprehensive change detection method for updating the National Land Cover Database to circa 2011. *Remote Sensing of Environment*, *132*, 159–175.

Julien, P. Y. (2010). *Erosion and Sedimentation.* 2nd ed. 385 pp. Cambridge University Press. UK.

Keane, R. E., Ryan, K. C., Veblen, T. T., Allen, C. D., & Logan, J. (2002). Cascading effects of fire exclusion in Rocky Mountain ecosystems: A literature review. *USDA Forest Service, Rocky Mountain Research Station. General Technical Report RMRS-GTR-91.*

Keeley, J. E. (2009). Fire intensity , fire severity and burn severity: a brief review and suggested usage. *International Journal Of Wildland Fire*, *18*, 116–126.

Krajewski, W. F., Vignal, B., Seo, B.-C., & Villarini, G. (2011). Statistical model of the range-dependent error in radar-rainfall estimates due to the vertical profile of reflectivity. *Journal of Hydrology*, *402*(3-4), 306–316.

Larsen, I. J., & MacDonald, L. H. (2007). Predicting postfire sediment yields at the hillslope scale: Testing RUSLE and Disturbed WEPP. *Water Resources Research*, *43*(11), 1-18.

Larsen, I. J., MacDonald, L. H., Brown, E., Rough, D., Welsh, M. J., Pietraszek, J. H., Libohova, Z., Benavides-Solorio, J., and Schaffrath, K. (2009). Causes of post-fire runoff and erosion: Water repellency, cover, or soil sealing? *Soil Science Society of America Journal*, *73*(4), 1393.

Legleiter, C. J., Kyriakidis, P. C., McDonald, R. R., & Nelson, J. M. (2011). Effects of uncertain topographic input data on two-dimensional flow modeling in a gravel-bed river. *Water Resources Research*, *47*(3), 1-24.

Legleiter, C. J., Lawrence, R. L., Fonstad, M. A., Marcus, W. A., & Aspinall, R. (2003). Fluvial response a decade after wildfire in the northern Yellowstone ecosystem: a spatially explicit analysis. *Geomorphology*, *54*(3-4), 119–136.

Limerinos, J. T. (1970). Determination of the Manning coefficient from measured bed roughness in natural channels. Geological Survey Water-Supply Paper 1898-B.

Lukas, J., Wolter, K., Mahoney, K., Barsugli, J., Doesken, N., Ryan, W., Ryan, W., Rangwala, I, Livneh, B., Gordon, E., Hoerling, M., and Kiladis, G. (2013). *Severe flooding on the Colorado Front Range: A preliminary assessment*. Western Water Assessment. 4 pp. Retrieved June 4, 2014, from http://coflood2013.colostate.edu/docs/wwa_assessment.pdf.

MacDonald, L. H., & Larsen, I. J. (2009). Effects of forest fires and post-fire rehabilitation: a Colorado case study. In A. Cerda & P. R. Robichaud (Eds.), *Fire Effects on Soils and Restoration Strategies.* 423–452. Enfield, NH.

Marks, K., & Bates, P. (2000). Integration of high-resolution topographic data with floodplain flow models. *Hydrological Processes*, *14*, 2109–2122.

Martin, W. (2013). WSR-88D dual polarization deployment progress. 6 pp. Retrieved August 13, 2014, from http://www.roc.noaa.gov/wsr88d/PublicDocs/DualPol/DPstatus.pdf.

Meyer, G. A., Pierce, J. L., Wood, S. H., & Jull, A. J. T. (2001). Fire, storms, and erosional events in the Idaho batholith. *Hydrological Processes*, *15*(15), 3025–3038.

Meyer, G. A., Wells, S. G., Balling Jr, R. C., & Jull, A. J. T. (1992). Response of alluvial systems to fire and climate change in Yellowstone National Park. *Nature*, *357*, 147–150.

Meyer, G. A., Wells, S. G., & Jull, A. J. T. (1995). Fire and alluvial chronology in Yellowstone National Park: climatic and intrinsic controls on Holocene geomorphic processes. *Geological Society Of America Bulletin*, *107*(10), 1211–1230.

Miller, A. J. (1995). Valley morphology and boundary conditions influencing spatial patterns of flood flow. In J. E. Costa, A. J. Miller, K. W. Potter, & P. R. Wilcock (Eds.), *Natural and Anthropogenic Influences in Fluvial Geomorphology, American Geophysical Union Geophysical Monograph, 89*. 57-81. Washington, D.C.

Miller, A. J., & Cluer, B. L. (1998). Modeling considerations for simulation of flow in bedrock channels. In E. E. Wohl & K. J. Tinkler (Eds.), *River Over Rock: Fluvial Processes in Bedrock Channels. American Geophysical Union Geophysical Monograph, 107.* 61-104. Washington, D.C.

Moody, J. A., & Martin, D. A. (2001a). Initial hydrologic and geomorphic response following a wildfire in the Colorado Front Range. *Earth Surface Processes and Landforms*, *26*(10), 1049–1070.

Moody, J. A., & Martin, D. A. (2001b). Post-fire, rainfall intensity-peak discharge relations for three mountainous watersheds in the western USA. *Hydrological Processes*, *15*(15), 2981–2993.

Moody, J. A., & Martin, D. A. (2009). Forest fire effects on geomorphic processes. In A. Cerdá & P. R. Robichaud (Eds.), *Fire Effects on Soils and Restoration Strategies2.* 41–79. Enfield, New Hampshire, USA: Science Publishers, Inc.

Moody, J. A., Martin, D. A., Haire, S. L., & Kinner, D. A. (2008). Linking runoff response to burn severity after a wildfire. *Hydrological Processes*, *22*, 2063–2074.

Morris, S. E., & Moses, T. A. (1987). Forest fire and the natural soil erosion regime in the Colorado Front Range. *Annals of the Association of American Geographers*, *77*(2), 245–254.

Neary, D. G., Klopatek, C. C., DeBano, L. F., & Ffolliott, P. F. (1999). Fire effects on belowground sustainability: a review and synthesis. *Forest Ecology and Management*, *122*(1-2), 51–71.

O'Connor, J. E., & Costa, J. E. (2004). Spatial distribution of the largest rainfall-runoff floods from basins between 2.6 and 26,000 km 2 in the United States and Puerto Rico. *Water Resources Research*, *40*(1), 1-11.

Onda, Y., Dietrich, W. E., & Booker, F. (2008). Evolution of overland flow after a severe forest fire, Point Reyes, California. *Catena*, *72*(1), 13–20.

Perica, S., Martin, D., Pavlovic, S., Roy, I., St. Laurent, M., Trypaluk, C., Unruh, D., Yekta, M., and Bonnin, G. (2013). NOAA Atlas 14: Precipitation-frequency atlas of the United States. *U.S. Department of Commerce and National Oceanic and Atmospheric Administration*.

Perron, T. (2013). TopoTools: Analysis of gridded elevation data in Matlab. Retrieved December 16, 2013, from http://web.mit.edu/perron/www/downloads.html.

Pietraszek, J. H. (2006). Controls on post-fire erosion at the hillslope scale, Colorado Front Range. M.S. Thesis. Department of Forest, Rangeland, and Watershed Stewardship. Colorado State University, Fort Collins, CO.

Rhoades, C. C., Entwistle, D., & Butler, D. (2011). The influence of wildfire extent and severity on streamwater chemistry, sediment and temperature following the Hayman Fire, Colorado. *International Journal of Wildland Fire*, *20*(3), 430-442.

Rinne, J. N. (1996). Short-term effects of wildfire on fishes and aquatic macroinvertebrates in the southwestern United States. *North American Journal of Fisheries Management*, *16*, 653–658.

Robichaud, P. R., Beyers, J. L., & Neary, D. G. (2000). Evaluating the effectiveness of postfire rehabilitation treatments. *USDA Forest Service, Rocky Mountain Research Station, Fort Collins, CO. General Technical Report RMRS-GTR-63.*

Roering, J. J., & Gerber, M. (2005). Fire and the evolution of steep, soil-mantled landscapes. *Geology*, *33*(5), 349.

Ryan, K. C., & Noste, N. V. (1985). Evaluating prescribed fires. *Proceedings - Symposium and Workshop on Wilderness Fire. USDA Forest Service Intermountain Forest and Range Experiment Station. General Technical Report INT-182.*, 230–238.

Ryzhkov, A. V, & Zrnic, D. S. (1996a). Assessment of rainfall measurements that uses specific differential phase. *Journal of Applied Meteorology*, *35*, 2080–2090.

Ryzhkov, A. V., & Zrnic, D. S. (1996b). Rain in shallow and deeep convection measured with a polarimetric radar. *American Meteorological Society*, *53*, 2990–2995.

Shakesby, R. a, & Doerr, S. H. (2006). Wildfire as a hydrological and geomorphological agent. *EarthScience Reviews*, *74*(3-4), 269–307.

Smith, J. A., Baeck, M. L., Meierdiercks, K. L., Nelson, P. A., Miller, A. J., & Holland, E. J. (2005). Field studies of the storm event hydrologic response in an urbanizing watershed. *Water Resources Research*, *41*(10), 1–15.

USACE. (2010). HEC-RAS river analysis system, User's Manual. *U.S. Army Corps of Engineeers, Hydrologic Engineering Center, Davis, CA*.

USACE. (2011). HEC-GeoRAS: GIS tools for support of HEC-RAS using ArcGIS, User's Manual. *U.S. Army Corps of Engineeers, Hydrologic Engineering Center, Davis, CA*.

Webb, R. H., & Jarrett, R. D. (2002). One-Dimensional Estimation Techniques For Discharges Of Paleofloods And Historical Floods. In *Ancient Floods; Modern Hazards: Principles and Applications of Paleoflood Hydrology; Water Science and Application, 5*. 111-125. American Geophysical Union. Washington, D.C.

Westerling, A. L., Hidalgo, H. G., Cayan, D. R., & Swetnam, T. W. (2006). Warming and earlier spring increase western U.S. forest wildfire activity. *Science*, *313*, 940–943.

Wohl, E. E. (1998). Uncertainty in flood estimates associated with roughness coefficient. *Journal of Hydraulic Engineering*, *124*(2), 219–223.

Wondzell, S. M., & King, J. G. (2003). Postfire erosional processes in the Pacific Northwest and Rocky Mountain regions. *Forest Ecology and Management*, *178*(1-2), 75–87.

Wright, D. B., Smith, J. A., Villarini, G., & Baeck, M. L. (2013). Long-Term High-Resolution Radar Rainfall Fields for Urban Hydrology. *Journal of the American Water Resources Association (JAWRA)*, 1–22.

8. APPENDIX

Table A1. Estimated discharge values for the slope-area method for the July 2012 flood

Manning's n	Pre-2013 flood discharge in cms (cfs)			Post 2013 flood discharge in cms (cfs)		
	XS2	XS9	XS10	XS2	XS9	XS10
0.03	23 (816)	22 (791)	38 (1342)	37 (1290)	47 (1672)	66 (2317)
0.04	17 (612)	17 (593)	29 (1007)	27 (968)	36 (1254)	49 (1737)
0.05	14 (490)	13 (474)	23 (805)	22 (774)	28 (1003)	39 (1390)
0.06	12 (408)	11 (395)	19 (671)	18 (645)	24 (836)	33 (1158)
0.07	10 (350)	10 (339)	16 (575)	16 (553)	20 (716)	28 (993)
0.08	9 (306)	8 (296)	14 (503)	14 (484)	18 (627)	25 (869)
0.09	8 (272)	7 (264)	13 (447)	12 (430)	16 (557)	22 (772)
0.10	7 (245)	7 (237)	11 (403)	11 (387)	14 (502)	20 (695)
0.11	6 (223)	6 (216)	10 (366)	10 (352)	13 (456)	18 (632)
0.12	6 (204)	6 (198)	10 (336)	9 (323)	12 (418)	16 (579)

Table A2. Discharge results for the slope-area method for the 2013 flood

Manning's n	Pre-2013 flood discharge in m^3/s (ft^3/s)				Post 2013 flood discharge in m^3/s (ft^3/s)			
	XS2	XS7	XS9	XS10	XS2	XS7	XS9	XS10
0.03	23 (816)	4 (129)	22 (791)	38 (1342)	37 (1290)	5 (175)	47 (1672)	66 (2317)
0.04	17 (612)	3 (97)	17 (593)	29 (1007)	27 (968)	4 (131)	36 (1254)	49 (1737)
0.05	14 (490)	2 (78)	13 (474)	23 (805)	22 (774)	3 (105)	28 (1003)	39 (1390)
0.06	12 (408)	2 (65)	11 (395)	19 (671)	18 (645)	2 (88)	24 (836)	33 (1158)
0.07	10 (350)	2 (55)	10 (339)	16 (575)	16 (553)	2 (75)	20 (716)	28 (993)
0.08	9 (306)	1 (48)	8 (296)	14 (503)	14 (484)	2 (66)	18 (627)	25 (869)
0.09	8 (272)	1 (43)	7 (264)	13 (447)	12 (430)	2 (58)	16 (557)	22 (772)
0.10	7 (245)	1 (39)	7 (237)	11 (403)	11 (387)	1 (53)	14 (502)	20 (695)
0.11	6 (223)	1 (35)	6 (216)	10 (366)	10 (352)	1 (48)	13 (456)	18 (632)
0.12	6 (204)	1 (32)	6 (198)	10 (336)	9 (323)	1 (44)	12 (418)	16 (579)

Table A3. RMSE values (m) computed by comparing water surface elevations computed in HEC-RAS with surveyed high water marks for the 2012 flood. Lowest RMSE values highlighted.

2012 flood discharge in m^3/s	Manning's n			
	0.04*	**0.06**	**0.08**	**0.10**
70	13.276	0.676	12.338	0.619
75	13.245	0.641	12.302	0.591
80	13.214	0.605	0.663	0.569
85	13.185	0.576	0.635	0.547
90	13.156	0.549	0.608	0.522
95	13.130	0.526	0.586	0.498
100	12.509	0.501	0.567	0.482
105	12.483	0.482	0.545	0.469
110	12.459	0.465	0.528	0.457
115	12.434	0.451	0.509	0.445
120	0.806	0.611	0.491	0.434
125	0.785	0.592	0.475	0.425
130	0.766	0.573	0.464	0.418
135	0.747	0.555	0.453	0.413
140	0.729	0.539	0.442	0.412
145	0.711	0.524	0.431	0.411
150	0.694	0.512	0.421	0.413
155	0.677	0.496	0.412	0.418
160	0.660	0.481	0.408	0.425
165	0.640	0.471	0.404	0.433
170	0.624	0.461	0.400	0.444
175	0.607	0.452	0.399	0.456
180	0.592	0.443	0.399	0.467
185	0.579	0.435	0.402	0.478
190	0.565	0.429	0.405	0.491
195	0.553	0.424	0.409	0.504
200	0.543	0.420	0.415	0.517
205	0.532	0.416	0.423	0.529
210	0.521	0.412	0.431	0.543
215	0.510	0.408	0.441	0.556
220	0.500	0.404	0.451	0.570
225	0.491	0.402	0.461	0.583
230	0.482	0.399	0.471	0.604
235	0.474	0.399	0.483	0.620
240	0.467	0.400	0.493	0.636

*Simulations of discharges greater than 240 m^3/s were not reported because the n=0.04 RMSE continued to decrease even to discharges in excess of 350 m^3/s.

Table A4. RMSE values (m) computed by comparing water surface elevations computed in HEC-RAS with surveyed high water marks for the 2013 flood. Lowest RMSE values highlighted.

Discharge in m^3/s	2013 pre-flood topography				2013 post-flood topography			
	Manning's n				Manning's n			
	0.04	0.06	0.08	0.10	0.04	0.06	0.08	0.10
5	23.074	0.631	0.556	0.501	1.190	1.021	1.038	0.986
10	0.586	0.446	0.360	0.280	1.044	0.821	0.851	0.774
15	0.459	0.301	0.197	0.117	0.944	0.672	0.708	0.615
20	0.340	0.187	0.098	0.081	0.859	0.554	0.586	0.487
25	0.268	0.110	0.080	0.113	0.784	0.435	0.488	0.377
30	0.212	0.090	0.101	0.178	0.719	0.336	0.401	0.278
35	0.184	0.116	0.139	0.259	0.658	0.247	0.320	0.195
40	0.165	0.135	0.200	0.333	0.598	0.210	0.246	0.169
45	0.148	0.176	0.268	0.391	0.542	0.247	0.184	0.179
50	0.152	0.224	0.328	0.448	0.491	0.249	0.156	0.219
55	0.164	0.250	0.374	0.504	0.439	0.214	0.163	0.231
60	0.172	0.287	0.423	0.553	0.392	0.164	0.172	0.258
65	0.189	0.326	0.467	0.603	0.349	0.148	0.210	0.325
70	0.205	0.338	0.510	0.646	0.307	0.156	0.219	0.386
75	0.229	0.393	0.550	0.688	0.265	0.173	0.237	0.436
80	0.248	0.409	0.586	0.733	0.235	0.206	0.278	0.483
85	0.276	0.444	0.622	0.779	0.226	0.228	0.350	0.529
90	0.294	0.464	0.655	0.817	0.223	0.245	0.404	0.575
95	0.314	0.495	0.689	0.855	0.225	0.278	0.441	0.618
100	0.335	0.541	0.726	0.892	0.250	0.314	0.479	0.665

Table A5: RMSE values (m) computed by comparing water surface elevations computed in Nays2D with surveyed high water marks for the 2012 flood. Lowest RMSE values highlighted.

2012 flood discharge in m^3/s	Manning's n			
	0.04	**0.06**	**0.08**	**0.10**
60	*	*	0.1721	0.1448
70	*	0.1627	0.1627	0.1443
80	*	0.1509	0.1390	0.1499
90	*	0.1428	0.1428	0.1706
100	0.1536	0.1345	0.1486	0.2094
110	0.1424	0.1410	0.1599	0.2400
120	0.1405	0.1413	0.1819	*
130	0.1489	0.1487	0.2117	*
140	0.1434	0.1569	0.2356	*
150	0.1580	0.1854	*	*

Table A6. RMSE values (m) computed by comparing water surface elevations computed in Nays2D with surveyed high water marks for the 2013 flood. Lowest RMSE values highlighted.

Discharge in m^3/s	2013 pre-flood topography				2013 post flood topography			
	Manning's n				Manning's n			
	0.04	**0.06**	**0.08**	**0.10**	**0.04**	**0.06**	**0.08**	**0.10**
5	*	0.085	0.078	0.070	*	*	*	*
10	0.074	0.062	0.071	0.086	*	0.119	0.115	0.110
20	0.071	0.114	0.156	0.188	0.109	0.101	0.086	0.059
30	0.072	0.172	0.236	*	0.088	0.062	0.062	0.103
40	0.106	0.226	0.344	*	0.068	0.070	0.125	0.208
50	*	*	0.470	*	0.066	0.117	0.213	*
60	*	*	*	*	0.073	*	*	*